iScience

CellPress
OPEN ACCESS

Article

Quantitative Conversion of Methanol to Methyl Formate on Graphene-Confined Nano-Oxides

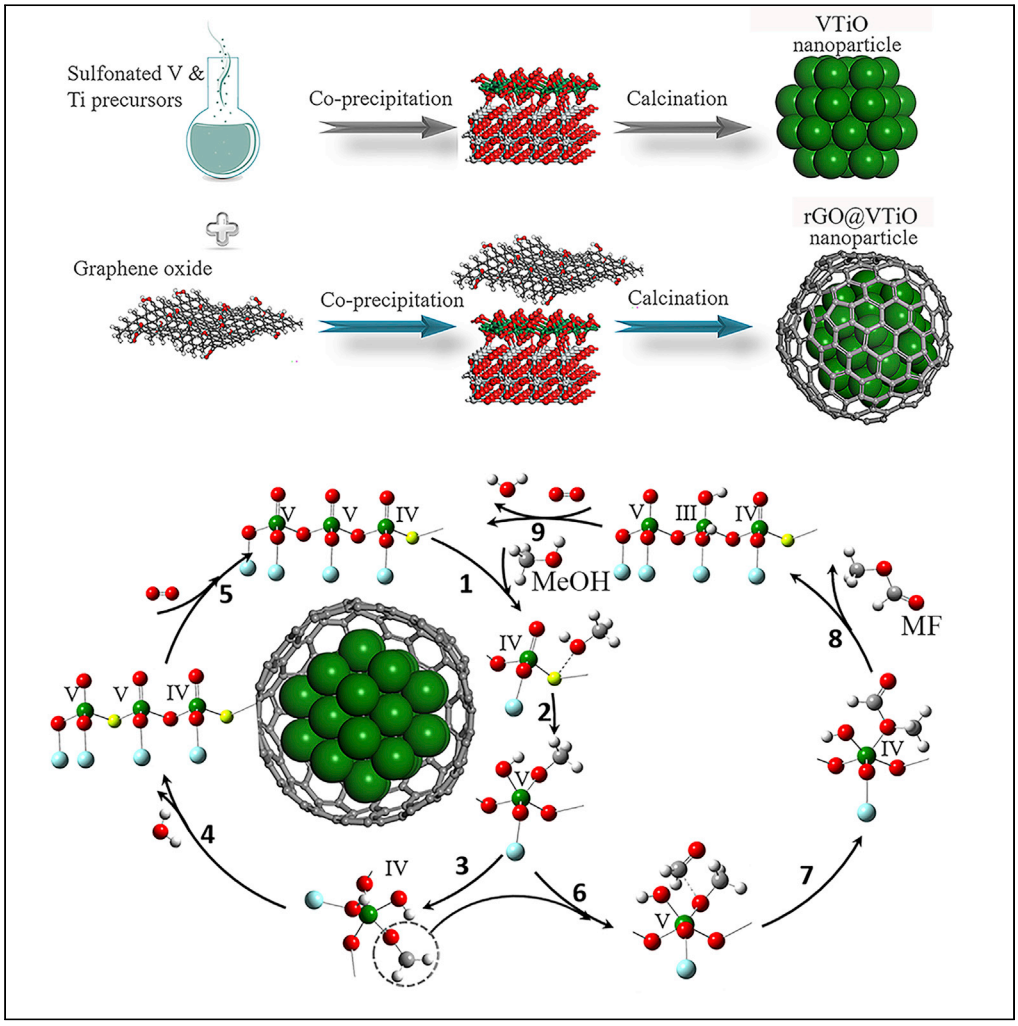

Yelei Zhang, Guojuan Liu, Lei Shi, ..., Nating Yang, Shenggang Li, Yuhan Sun

zenggf@sari.ac.cn (G.Z.)
lisg@sari.ac.cn (S.L.)

HIGHLIGHTS

Reduced-graphene-oxide-confined VTiOx nanoparticles (rGO@VTiO) were developed

Nearly 100% conversion of methanol to methyl formate was achieved

rGO interacts strongly with the inner species

Acidity of rGO@VTiO was significantly enhanced without sulfates

Zhang et al., iScience *23*, 101157
June 26, 2020
https://doi.org/10.1016/j.isci.2020.101157

iScience

CellPress
OPEN ACCESS

Article

Quantitative Conversion of Methanol to Methyl Formate on Graphene-Confined Nano-Oxides

Yelei Zhang,[1,2,5] Guojuan Liu,[1,5] Lei Shi,[1,5] Ping Wu,[1] Gaofeng Zeng,[1,2,6,*] Chunlei Zhang,[1,3] Nating Yang,[1] Shenggang Li,[1,4,*] and Yuhan Sun[1,4]

SUMMARY

We demonstrate the nearly quantitative conversion of methanol to methyl formate (MF) with a reliable durability on the reduced-graphene-oxide-confined VTiOx nanoparticles (rGO@VTiO). The rGO@VTiO exhibits superior low-temperature reactivity than the rGO-free VTiO, and the MF yield of 98.8% is even comparable with the noble metal catalysts. Both experiments and simulations demonstrate that the ultrathin rGO shell significantly impacts the shell/core interfacial electronic structure and the surface chemistry of the resultant catalysts, leading to remarkable reactivity in methanol to MF. rGO enhances the dispersion and loading rates of active monomeric/oligomeric VOx. In particular, the electron migration between the rGO shell and oxides core reinforces the acidity of rGO@VTiO in the absence of sulfate acidic sites. Moreover, both *in situ* NAP-XPS and DRIFTS investigations suggest that the lattice oxygen was involved in the oxidation of methanol and the MF was formed via the hemiacetal mechanism.

INTRODUCTION

Methyl formate (MF) is an important building block molecule in synthetic chemistry and a versatile antiseptic and solvent as well (Zeng et al., 2019; Banerjee and Kanan, 2018; Zhang et al., 2019). It is commercially produced by the sodium methoxide-catalyzed methanol carbonylation with CO, which poses severe environmental concerns owing to the toxic and corrosive reagents (Kaichev et al., 2014; Zhang et al., 2019). Thus, there are significant interests in developing more efficient and greener processes for MF synthesis. Direct oxidative coupling of methanol to MF over the supported noble metal or transition metal oxide catalysts is a simple, non-corrosive, and economical process (Whiting et al., 2015; Wang et al., 2013; Wittstock et al., 2010; Zhang et al., 2014a, 2014b). Among the catalysts, TiO_2-supported vanadia (VTiO) was widely studied because it is more available than the noble metal catalysts and more reactive than most of the non-precious catalysts (Zhao et al., 2010a, 2010b; Kaichev et al., 2014; Liu et al., 2016). However, it is generally difficult to simultaneously achieve high MF selectivity together with high methanol conversion, leading to a low single-pass yield of MF. In view of the deep oxidation of methanol to CO_2 as well as the explosion risk, moreover, it is also critical to reduce the reaction temperature. Therefore, further improving the MF yield at lower temperature is highly desired for the VTiO-based catalysts.

Graphene is a 2D atomic crystal with sp2-hybridized carbon, which possesses unique electronic, chemical, and mechanical properties and therefore has been investigated for wide applications including catalysis (Li et al., 2015; Deng et al., 2016; Wang et al., 2019). As a catalyst, graphene takes the advantages of large surface area, excellent mechanical properties, and high thermal/electron conductivities (Deng et al., 2016). In particular, the dislocations, vacancies, edges, impurities, and functional groups of graphene can all promote its catalytic properties (Tang et al., 2019). Graphene-encapsulated metal particles (e.g., Pt) have exhibited superior activities for the reactions like methane oxidation and electrocatalysis of water oxidation (Cui et al., 2018; Deng et al., 2017). With embedding single iron atoms into the graphene matrix, moreover, it offered impressive activity in the selective oxidation of benzene and methane at room temperature (Cui et al., 2018; Deng et al., 2015). For these graphene-confined metal catalysts, the electrons of metal atoms can penetrate through the graphene shell to promote the catalytic reaction, whereas the graphene shell can protect the inner metals from damage in reaction (Deng et al., 2013a). Potentially, the excellent oxidation activities and low-temperature properties of such graphene@metal catalysts inspire us to develop more efficient catalyst for methanol oxidation to MF. However, the catalyst of graphene-confined metal oxides has not been demonstrated.

[1]CAS Key Laboratory of Low-carbon Conversion Science and Engineering, Shanghai Advanced Research Institute, Chinese Academy of Sciences, Shanghai 201210, China

[2]School of Chemical Sciences, University of Chinese Academy of Science, Beijing 100049, China

[3]School of Environmental and Chemical Engineering, Shanghai University, 99 Shangda Road, Shanghai 200444, China

[4]School of Physical Science and Technology, ShanghaiTech University, Shanghai 201210, China

[5]These authors contributed equally

[6]Lead Contact

*Correspondence: zenggf@sari.ac.cn (G.Z.), lisg@sari.ac.cn (S.L.)

https://doi.org/10.1016/j.isci.2020.101157

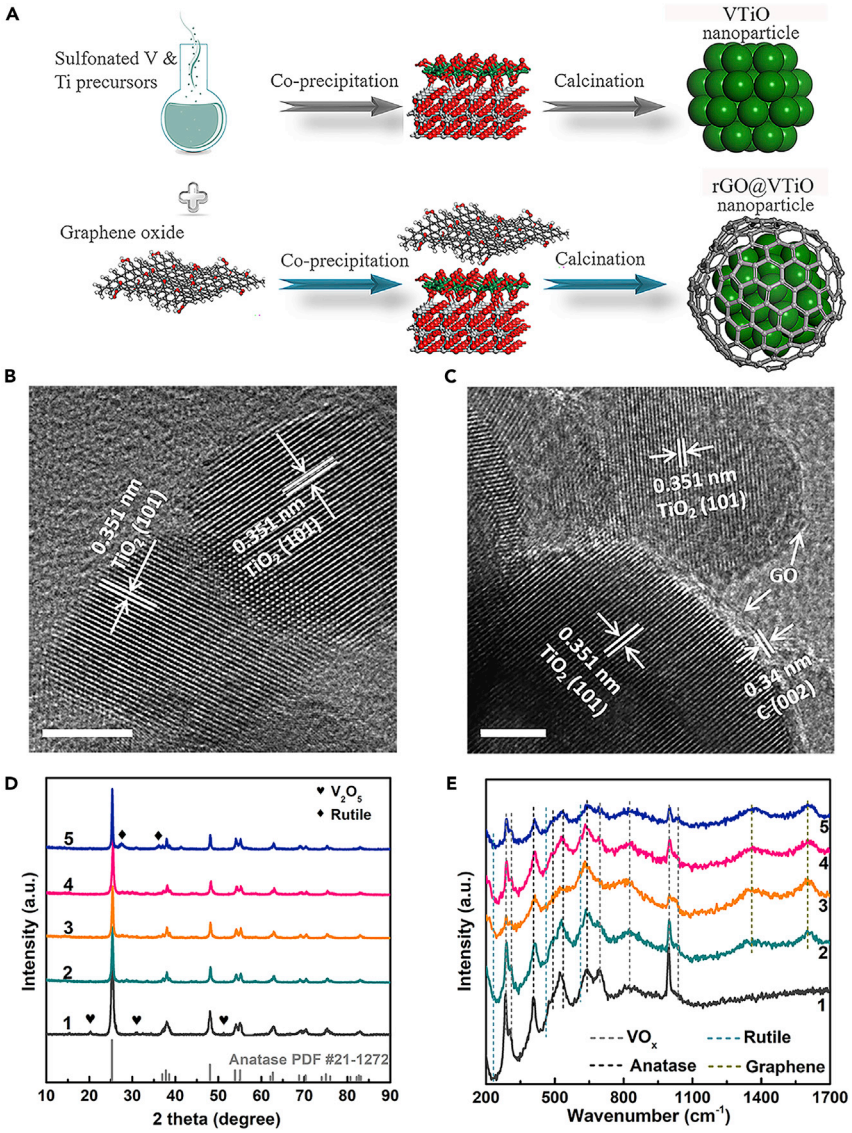

Figure 1. Preparation Procedure of Catalyst and the Structural Analysis of Catalysts

(A–E) (A) Schematic of VTiO and rGO@VTiO preparation; TEM images of VTiO (B) and 0.6(rGO)@VTiO (C); (D) XRD patterns and (E) Raman spectra of n(rGO)@VTiO n = 0 (**1**), 0.3 (**2**), 0.6 (**3**), 1.0 (**4**), and 2.0 (**5**). Scale bar is 5 nm.
See also Figures S1–S6 and Table S1.

Herein, we developed the reduced GO (rGO)-encapsulated VTiOx catalyst (rGO@VTiO) through a facile co-precipitation method. Over these catalysts, not only nearly quantitative conversion of methanol to MF was achieved but also the low-temperature activity was highly improved. Effects of the ultrathin rGO shell on the structure and surface chemistry of the catalyst as well as the reaction mechanism were thoroughly investigated by experiments and computations.

RESULTS

rGO Impacts on the Structure and Texture of Catalysts

The *n*(rGO)@VTiO catalysts were prepared through co-precipitating the acidic aqueous mixture of $VOSO_4$, $TiSO_4$, H_2SO_4, and GO suspension with ammonia solution, where *n* refers to the weight percentage of GO used in the preparation recipes. As control, the sulfated VTiO catalysts were fabricated using the same method without GO addition (Figure 1A). The transmission electron microscope (TEM) images show the microstructure of VTiO and rGO@VTiO. VTiO sample displayed clean and clear particle boundaries with

the well-ordered microstructure that can be assigned to the anatase TiO_2 (101) (Figure 1B).(Sima et al., 2017) For 0.6(rGO)@VTiO, the VTiO particles were isolated and well encapsulated by the rGO layer, and the cross-sectional view indicated that most of the layer is around 1.5 nm thick (Figures 1C and S1). As the rGO mono-sheet is 0.4–0.7 nm thick (depends on the reduction degree of GO), the number of rGO mono-sheet on 0.6(rGO)@VTiO is 2–4 (Yang et al., 2018; Qi et al., 2017). Similarly, the rGO shells were also observed from other *n*(rGO)@VTiO samples (*n* = 0.3, 1.0, 2.0) (Figure S2). Both measurements and simulations have suggested that the electron shuttle across the graphene is limited to <4 carbon layers and the thinner graphene layer can enhance the adsorption and reduction of O_2 owing to the promoted electron transfer inside catalyst (Deng et al., 2013b). Therefore, the ultrathin rGO shell with ~3 carbon layers on 0.6(rGO)@VTiO may contribute to the physicochemical properties of catalyst.

In addition, rGO increased the surface area of catalysts, in which the Brunauer-Emmett-Teller (BET) specific surface area grew from 46 $m^2\ g^{-1}$ of VTiO to 121 $m^2\ g^{-1}$ of 0.6(rGO)@VTiO, for example (Table S1). The larger surface area improved the surface dispersion of vanadium species, as evidenced by the elemental analysis. The overall V/Ti ratio of catalysts determined by the inductively coupled plasma atomic emission spectrometry (ICP-AES) slightly increased from 0.24 of VTiO to 0.31 of rGO@VTiO (Table S1), suggesting that rGO improved the loading rate of V species. The near- and sub-surface V/Ti measured by X-ray photoelectron spectroscopy (XPS) and energy dispersive spectrometer (EDS), respectively, were higher than that of the bulk catalysts, indicating the surface enrichment of vanadium species. At the same time, the near-surface V/Ti decreased from 0.41 for VTiO to 0.33–0.36 for rGO@VTiO samples owing to the larger surface area and the higher V dispersion on rGO@VTiO than that on VTiO (Table S1). On the other hand, the elemental mapping of rGO@VTiO revealed that V, Ti, and C were uniformly distributed on the sample (Figure S3).

As proved by XPS, EDS, and CHNS elemental analyzer, interestingly, the sulfur content decreased with the increase of rGO and closed to 0 for the samples of 0.6/1.0/2.0(rGO)@ VTiO (Table S1). It is reasonable that the deposition of SO_4^{2-} was suppressed during the catalyst precipitation owing to the electrostatic repulsion between GO and SO_4^{2-} (Qi et al., 2017). Furthermore, the carbonyl groups on GO are enable to react with sulfur-centered anions during the catalyst calcination, resulting in the loss of sulfur (Gu et al., 2017; Li et al., 2016; Zhu et al., 2015). Since the acidity is vital for the catalytic oxidation of methanol to MF, the sulfation is an efficient method to enhance the acidity of VTiO-based catalysts (Zhang et al., 2019). But the sulfate groups are unstable upon the calcination and reaction conditions owing to their weak interactions with VTiO, which is always challenging the durability and reactivity of sulfated VTiO catalysts (Liu et al., 2016). In view of the superior reactivity of rGO@VTiO hereinafter, however, it indicates that their acidities were well improved even in the absence of sulfur, which will be proved by the acidity analysis.

The crystal structure of catalysts was measured by XRD (Figure 1D). Apart from anatase TiO_2, the V_2O_5 crystals were also observed from the pattern of VTiO due to the aggregation of vanadia species, in line with the elemental distribution analysis of catalyst surface. However, V_2O_5 was undetectable from the 0.3, 0.6, and 1.0(rGO)@VTiO samples. This confirms that rGO promoted the dispersion of the vanadia species and suppressed the growth of crystalline V_2O_5. For 2.0(rGO)@VTiO, on the other hand, the thickened GO layer may impede the thermal transfer and elevate the real temperature of inner particles during the isothermal calcination of catalyst, leading to the formation of rutile TiO_2 (Figure 1D). As references, GO pattern exhibited a typical peak at ~12° assigned to GO (001), whereas the thermal reduced rGO only displayed a wide peak of graphite (002) at ~26° (Figure S4) (Yang et al., 2018). It reveals that GO was well reduced to rGO under the conditions of catalyst calcination, which was further supported by XPS and IR results that the C/O ratio increased from 3.2 of GO to 11.0 of rGO and the bands of O-containing groups of rGO significantly weakened (Figures S5 and S6).

The structures of rGO@VTiO and VTiO were checked by Raman spectroscopy (Figure 1E). The bands at 404, 507, 521, and 640 cm^{-1} were attributed to Ti-O groups of anatase TiO_2. For 1.0/2.0(rGO)@VTiO, the additional weak peaks at 243, 446, and 609 cm^{-1} assigned to rutile TiO_2 (Sima et al., 2017), in line with the XRD results. The bands at 284, 303, 697, and 997 cm^{-1}, ascribed to crystalline V_2O_5 (Zhao et al., 2010b), were gradually weakened with the rGO contents and then slightly increased for 1.0/2.0(rGO)@VTiO. This is consistent with the XRD observations that the optimal amount of rGO suppressed the formation of V_2O_5. Moreover, a new band around 1,034 cm^{-1}, assigned to the polymeric VO_x, appeared in rGO@VTiO samples and a broad band at 820 cm^{-1} assigned to the isolated VO_4 tetrahedral increased in intensity for

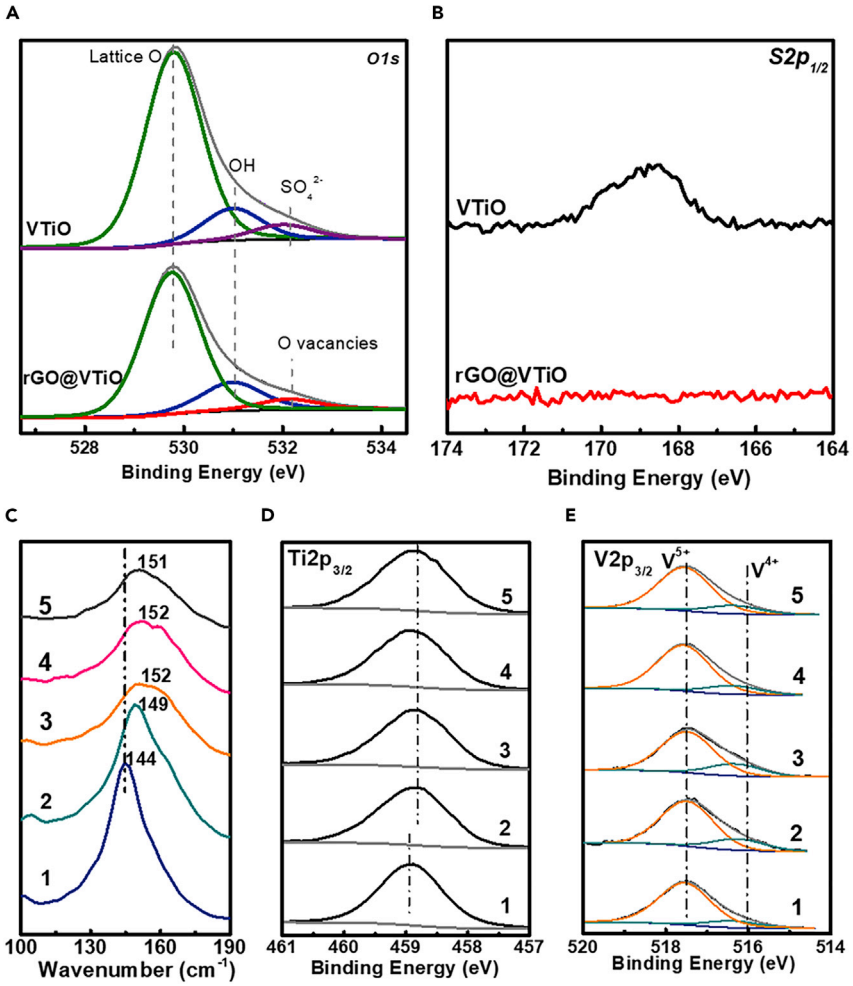

Figure 2. Surface Chemistry of rGO@VTiO-Based Catalysts

(A–E) (A) O1s and (B) $S2p_{1/2}$ XPS spectra of VTiO and 0.6(rGO)@VTiO; (C) Raman spectra, (D) $Ti2p_{3/2}$, and (E) $V2p_{3/2}$ XPS spectra of n(rGO)@VTiO n = 0 (**1**), 0.3 (**2**), 0.6 (**3**), 1.0 (**4**), and 2.0 (**5**).

See also Table S2.

0.3/0.6(rGO)@VTiO (Zhang et al., 2019; Sima et al., 2017). It confirms that vanadium species mainly exist as crystalline V_2O_5 in VTiO but partial vanadium transformed into monomeric/polymeric VO_x for rGO@VTiO owing to the high dispersion. Furthermore, two characteristic peaks around 1,350 and 1,600 cm^{-1}, assigned to the D band (from in-plane imperfections such as defects and heteroatoms of the graphitic lattice of the disordered sp2-hybridized carbon) and G band (from the tangential stretching mode of highly ordered pyrolytic graphite), respectively, were detected from the rGO@VTiO samples, which confirms the existence of rGO in the samples (Figure 1E).

rGO Impacts on the Chemistry of Catalysts

The surface chemistry of the catalysts was measured by XPS. As shown in Figure 2A, the O1s spectrum of VTiO was composed by three peaks centered at 529.7 (lattice oxygen), 531.0 (oxygen of -OH), and 531.9 eV (sulfate oxygen species) (Zhao et al., 2010b). The binding energy of S2p spectrum at 169.1 eV was ascribed to SO_4^{2-} for VTiO but no sulfur was detectable for 0.6(rGO)@VTiO (Figure 2B), confirming the sulfur loss in 0.6(rGO)@VTiO. Thus, the O1s peak of 0.6(rGO)@VTiO at 532.1 eV is assigned to the oxygen vacancy (OV) rather than SO_4^{2-} (Figure 2A) (Wan et al., 2018). The state of OVs was further evinced by Raman spectra (Figure 2C). The E_g mode of TiO_2 shifted from 144 cm^{-1} of VTiO to 151 $\pm$ 2 cm^{-1} for rGO@VTiO owing to the formation of OVs (Wang et al., 2018a). Reasonably, the OV formation is relevant to the interactions between rGO ultrathin-shell and VTiO nanoparticles.

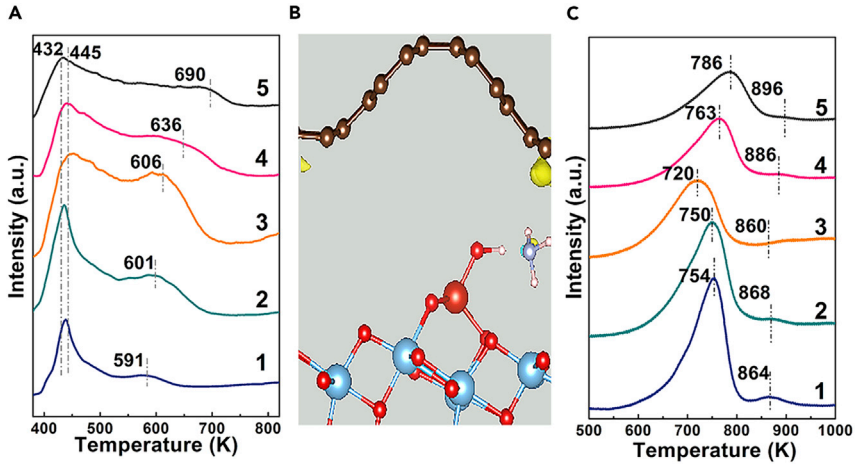

Figure 3. Acidity and Redox Properties of rGO@VTiO-Based Catalysts

(A) NH_3—TPD profiles of n(rGO)@VTiO n = 0 (**1**), 0.3 (**2**), 0.6 (**3**), 1.0 (**4**), and 2.0 (**5**).

(B and C) (B) Electron density difference of NH_3 adsorption on the interface of rGO@VTiO (C, brown; Ti, blue; O, red; N, light blue; H, white. Dark blue and yellow contours refer to the electron depletion and electron accumulation, respectively. The isosurface levels are set to be 0.001 e/Bohr^3) and (C) H_2—TPR profiles of samples **1–5**.

See also Figures S7 and S8 and Tables S3 and S4.

The carbonyl groups of GO could interact with the activated O_2 molecules and then attack the adjacent sulfur groups (Gu et al., 2017). Instead of O_2, it is also fair that the surface lattice oxygen of VTiO interact with the carbonyl groups of GO and then trigger the desulfurization during the catalyst calcination in N_2, leading to sulfur loss and OV formation. In principle, the OV formation would reduce the metal valence, as confirmed by Ti2p and V2p spectra. The binding energies of Ti2p3/2 slightly down-shifted from 459.0 eV of VTiO to 458.7 eV of rGO@VTiO (Figure 2D), indicating a small amount of Ti^{4+} changed to Ti^{3+} (Kaichev et al., 2014). Similarly, V^{4+} proportions increased from 21.8% for VTiO to 26.5%–33.6% for rGO@VTiO samples (Figure 2E and Table S2). Since OVs possess high adsorption and activity for O_2, it is reasonable to enhance the reactivity in methanol oxidation.

Bifunction of redox and acidity is the key character to promote the partial oxidation of methanol to MF (Zhao et al., 2010a). As shown in Figure 3A, the temperature-programmed desorption of ammonia (NH_3-TPD) profiles of VTiO and rGO@VTiO displayed two desorption peaks of NH_3 at 430–450 K and 590–690 K, corresponding to the weak and medium-strong acidic sites, respectively (Lu et al., 2011). For VTiO, the residual sulfate groups significantly impact its acidity (Sima et al., 2017). With the increase of rGO, the medium-strong acid gradually up-shifted from 591 K of VTiO to 601–690 K for rGO@VTiO samples. The peak areas of weak and medium-strong acid significantly increased from 808 to 389 of VTiO to 1,884 and 1,324 of 0.6(rGO)@VTiO and then decreased to 1,206 and 625 for 2.0(rGO)@VTiO, respectively (Table S3). This reveals that the moderate rGO improved the acidity, whereas the excessive rGO might cover the acidic sites. 0.6(rGO)@VTiO contained the most acidic sites, which is consistent with its reactivity in the methanol oxidation. The acidity of VTiO and 0.6(rGO)@VTiO was further measured by pyridine adsorption infrared spectroscopy (Figure S7). The bands at 1,612 and 1,452 cm^{-1} correspond to Lewis acid sites, whereas the band at 1,545 cm^{-1} is attributed to Brønsted acid sites. The bands around 1,490 and 1,574 cm^{-1} are ascribed to the overlapping of Brønsted and Lewis acid sites. The enhanced signal intensities from 0.6(rGO)@VTiO confirmed that its acidity was significantly improved with interaction between rGO and VTiO, in line with the NH_3-TPD results. As a control, the NH_3-TPD results of rGO exhibited negligible acidity (Figure S8). Since it has been confirmed that sulfate groups were almost free in rGO@VTiO, the notably enhanced acidity of rGO@VTiO is evidently contributed by the interactions between rGO and VTiO rather than the sulfate groups and/or the rGO itself.

The effects of rGO on the acidity of rGO@VTiO were further simulated (Figure 3B). The intercalation of NH_3 molecule leads to a significant electron migration and accumulation on the graphene surface. The simulation indicates that NH_3 adsorption is stronger on rGO@VTiO than on VTiO (−0.89 versus −0.77 eV), which aligns with the NH_3-TPD results. In rGO@VTiO, the curled graphene offers electrons to the inner particles

and displays a different electron density between the outer/inner surfaces, which further enhances the density of states near the Fermi level of graphene and therefore increases the number of acidic sites (Deng et al., 2013a).

The redox properties of the catalysts were studied by hydrogen temperature-programmed reduction (H_2-TPR) (Figure 3C). The reduction temperature downshifted from 754 K of VTiO to 720 K of 0.6(rGO)@VTiO and then increased to 786 K for 2.0(rGO)@VTiO. This corresponds to the different types of VO_x species. In a high dispersion state, monomeric VO_x groups with three V-O bonds to TiO_2 and a terminal partly hydrated V=O bond would be formed (Bulushev et al., 2002). Upon the enrichment of V species, some V-O-Ti bridges rearranged into V-O-V polymerization bridges, which turn to crystalline V_2O_5 with further increasing V coverage (Sima et al., 2017). In general, the monomeric and polymeric VO_x species are easier to be reduced than crystalline V_2O_5 (Bulushev et al., 2002). Therefore, 0.6(rGO)@VTiO displayed the lowest reduction temperature owing to the high content of monomeric/polymeric VO_x, whereas VTiO displayed higher reduction temperature owing to more crystalline V_2O_5. This agrees well with the XRD, XPS, and Raman measurements. Moreover, the easier reduction of 0.6(rGO)@VTiO is consistent with its low-temperature reactivity in methanol to MF. Meanwhile, the peak area gradually decreased with the increase of rGO in the catalysts (Table S4), as the formation of OVs decrease the H_2 consumption. On the other end, the small peaks centered at 860–896 K, ascribed to the reduction of sulfate species (Liu et al., 2016), rapidly decreased in the peak area from 50 for VTiO to <4 for rGO@VTiO (Table S4), which verifies again its sulfur loss.

rGO Impacts on the Methanol Oxidative Coupling

The explosion proof is the principal concern in the real practice of catalytic oxidation (Figure S9). However, the available explosive limits of methanol-oxygen (air) systems were derived from the ambient temperature and pressure, which is imprecise for the real oxidation. Thus, the real explosive limits of methanol-O_2-N_2 were recorded by an alternating current center-fire method at 423 K and 3 bar (Figure 4A). Correspondingly, the methanol oxidation on our catalysts was conducted under a safe envelope.

Methanol oxidation on 0.6(rGO)@VTiO and the reference samples were tested in a micro-fixed-bed reactor at 388 to 423 K (Figure 4B). The optimized feeding conditions, P = 0.1 MPa, $N_2/O_2 = 9$, $O_2/CH_3OH = 1.5$, and GHSV = 3,000 h^{-1}, were used for the oxidation test (Table S5). With temperature increasing, the methanol conversion (C_{MeOH}) on VTiO increased from 63.2% to 96.2%, whereas the MF selectivity (S_{MF}) exhibited a peak value of 93.0% at 408 K, reflecting the MF yields (Y_{MF}) from 47.5% at 388 K to the maximum of 88.7% at 413 K. As a control, rGO showed a poor reactivity that the inferior C_{MeOH} (<36%) and S_{MF} (<27%) derived to Y_{MF} < 9% at 388–423 K. In contrast, 0.6(rGO)@VTiO offered superior reactivity for methanol to MF. A Y_{MF} of 88.0%, translated from C_{MeOH} of 91.0% and S_{MF} of 96.7%, was obtained even at 388 K, which is 85% higher than that on VTiO (i.e., Y_{MF} = 47.5%). This demonstrates an enhanced low-temperature reactivity of rGO@VTiO. Then C_{MeOH} exceeded 99.0% at 403 K and further closed to complete conversion (99.8%) at 413 K. Meanwhile, S_{MF} increased to >99.0% at 403–408 K. Correspondingly, Y_{MF} = 98.8% was obtained even at 408 K on 0.6(rGO)@VTiO. On the other hand, the Y_{MF} of 0.3/1.0(rGO)@VTiO were higher than that of VTiO but slightly lower than that of 0.6(rGO)@VTiO (Figure S10). It suggests that the appropriate amount of rGO in the catalyst tends to significantly improve its reactivity in methanol to MF.

The CO_2 selectivity (S_{CO2}) on the catalysts were shown in Figure 4C. For rGO, CO_2 was undetectable at 388–413 K and then slightly increased to 0.5%–1.3% at $\geq$ 418 K. This indicates that rGO itself is chemically stable with poor activity for methanol conversion, in line with its MF yields. However, it is much easier to generate CO_2 on VTiO even at 403 K and the S_{CO2} reached 8% at 423 K. In contrast, S_{CO2} was significantly suppressed on 0.6(rGO)@VTiO. No CO_2 can be detected until 418 K, implying that rGO restrains the deep oxidation of methanol. The long-term stability of 0.6(rGO)@VTiO was investigated at 408 K (Figure 4D). Both C_{MeOH} and S_{MF}, averaging at 99.7 $\pm$ 0.2% and 99.1 $\pm$ 0.3%, respectively, remain stable with slight fluctuations during 500-h testing, demonstrating a reliable catalytic stability with high reactivity.

The oxidation of methanol to MF on 0.6(rGO)@VTiO was compared with those on the various catalysts under their optimized conditions (Han et al., 2014; Whiting et al., 2015; Wang et al., 2013; Wittstock et al., 2010; Zhang et al., 2014a, 2014b), as summarized in Figure 4E and Table S6. Owing to the high reactivity of the noble metal-containing catalysts, methanol can be converted into MF at relatively low temperature. Among the noble metal catalysts, the highest MF yield of ~90% was obtained on the Au-Pd nanoparticles

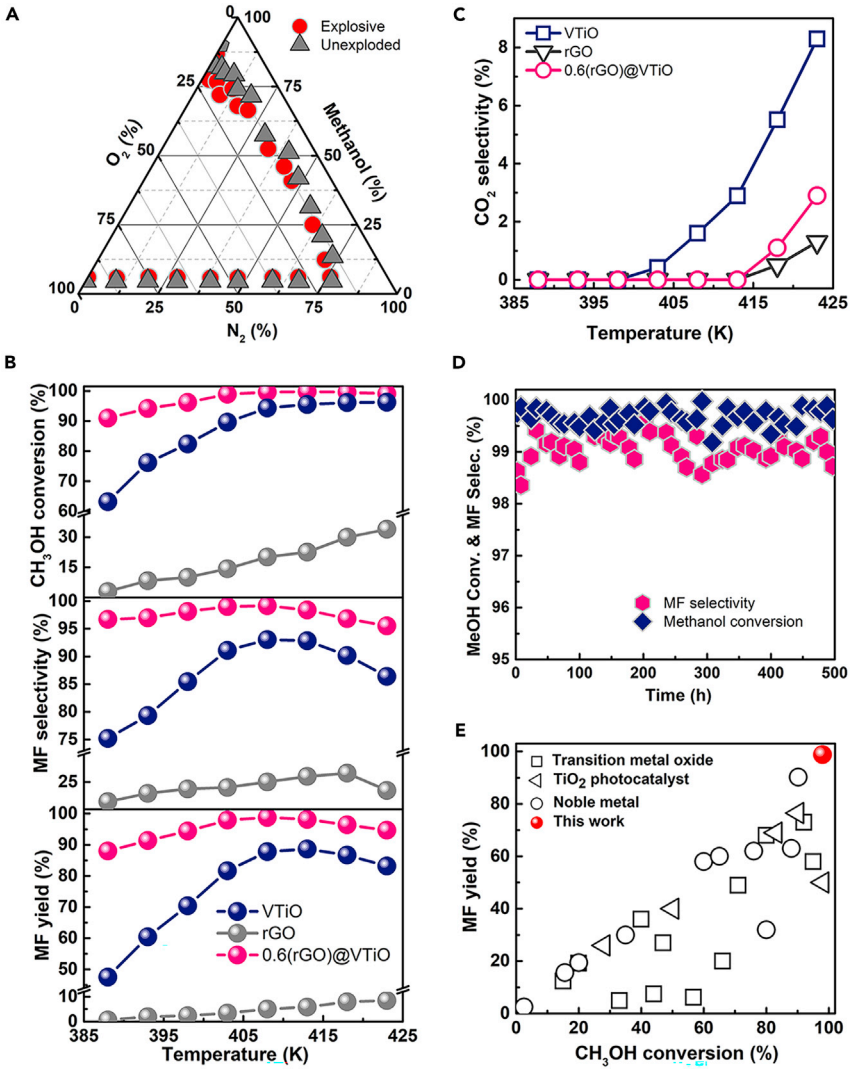

Figure 4. Selective Oxidation of Methanol to MF on rGO@VTiO Based-Catalysts

(A–C) (A) The explosibility of O_2-MeOH-N_2 system (423 K, 3 bar, alternating current 7 kV center fire); temperature dependence of (B) methanol conversion, MF selectivity and yield, and (C) CO_2 selectivity on VTiO, rGO, and 0.6(rGO)@VTiO catalysts (GHSV = 3000 mL $gcat^{-1}$ h^{-1}).

(D) Stability of 0.6(rGO)@ VTiO at 408 K.

(E) Comparison of methanol oxidation to MF on 0.6(rGO)@VTiO with various catalysts.

See also Figures S9 and S10 and Tables S5 and S6.

at 343 K (Wang et al., 2013). TiO_2-supported Au-Ag offered the highest MF yield of 77.0% at room temperature in photo-catalysis of methanol (Han et al., 2014). However, the high cost of noble metals limits their application. The non-noble oxide catalysts, like ReO_x/CeO_2, V_2O_5/TiO_2, and RuO_x-ZrO_2, are more accessible, but they present much lower reactivity for the methanol conversion even at high temperature. Evidently, 0.6(rGO)@VTiO exhibited higher single-pass MF yield compared with these catalysts including noble metals. Compared with the sulfated VTiO, obviously, 0.6(rGO)@VTiO demonstrated excellent low-temperature activity, methanol conversion, and MF selectivity. In methanol to MF, the over-oxidation of methanol to CO_x, which normally depends on the reaction temperature, should be avoided as far as possible to increase the usage of methanol. To lower the difficulty of product purification, moreover, it requires high yield of target product. Therefore, rGO@VTiO exhibits the high reactivity at low temperature, which not only suppresses the complete oxidation of methanol but also relieves the challenge of product separation.

In Situ NAP-XPS and IR of Methanol Oxidation on rGO@VTiO

To gain insights into the reaction, 0.6(rGO)@VTiO was measured *in situ* near atmospheric pressure XPS (NAP-XPS) under the simulated reaction conditions. In pure methanol, V^{5+} weighted >70% of vanadium at 303–353 K and then V^{4+}% grew at higher temperature (e.g., V^{4+}% = 42.6% at 373 K) (Figure 5A and Table S7). Moreover, a new peak at 515.3 eV ascribed to V^{3+} appeared at 393 K and more V^{4+} + V^{3+} were formed above 393 K, leaving only 26.7% of V^{5+} at 473 K. The reduction of V^{5+} to V^{4+}/V^{3+} corresponds to the chemisorption and oxidation of methanol on the catalyst (Odriozola et al., 1991). As a comparison, the appearance of V^{3+} on VTiO is 20 K higher (Figure S11 and Table S8). This reveals that rGO@VTiO possesses superior low-temperature activity for methanol adsorption and activation, in line with the real reaction.

The thermal effects on the activation of O_2 over 0.6(rGO)@VTiO and VTiO were checked in methanol + O_2 mixture at 303–473 K (Figure S12). The increased V^{5+}% reveals that O_2 was activated and replenished on catalysts. However, 0.6(rGO)@VTiO possesses higher V^{4+}% than VTiO (Table S9), indicating that it can activate more O_2.

The effects of O_2 partial pressure were tested using 0–0.6 mbar O_2 mixed with 0.4 mbar methanol at 403 K (Figure 5B and Table S10). With the presence of O_2, V^{3+} rapidly converted into higher valence states and the ratios of V^{5+}/V^{4+} increased with the O_2 pressure. The V^{4+} fractions of 0.6(rGO)@VTiO were higher than those of VTiO under the same conditions (Figure S13 and Table S11). This confirms that rGO enhanced the redox capacity of catalysts, in line with the H_2-TPR results. It has been proposed that O_2 can adsorb and be activated on graphene (Deng et al., 2013a)' (Deng et al., 2015b) In rGO@VTiO, the electron transfer between rGO shell and nanoparticles may decrease the local work function of graphene surface, which promotes the adsorption and activation of O_2 on rGO. Thus, it enhanced the oxygen migration and the availability of the oxygen atom in the bridging V-O-Ti bond and thus improves the redox capability of catalyst (Deng et al., 2013a) (Liu et al., 2009), Therefore, rGO@VTiO possesses superior low-temperature activity in comparison with VTiO owing to the interactions between rGO shell and inner oxides.

Figure 5C displays the corresponding C1s spectra of 0.6(rGO)@VTiO in pure methanol at 323–473 K. The deconvoluted peaks ascribed to graphite C-C (285.1 $\pm$ 0.1 eV), methoxy species C-O (286.3 $\pm$ 0.1 eV), dioxymethylene (287.5 eV), gas-phase methanol (287.9 $\pm$ 0.2 eV), and formate species and MF (288.9 eV), respectively (Romanyshyn et al., 2008). The amount of the methoxy species initially increased with temperature in 303–393 K and then gradually decreased at higher temperatures (Table S12). Simultaneously, the signals of dioxymethylene and formate species increased with temperature. This confirms that the elevated temperature promotes the chemisorbed methanol to form methoxy groups, whereas the further higher temperature triggers the conversion of methoxy to formate species. The peak assigned to dioxymethylene increased rapidly from 17.2% in pure methanol to 28.5% in 0.1 mbar O_2 + methanol at 403 K (Figure 5D and Table S13). It reveals that methoxy was rapidly oxidized to dioxymethylene with little O_2. Increasing O_2 pressure, more MF was detected while dioxymethylene decreased, suggesting O_2-rich condition was favorable to form MF (Zhang et al., 2019).

To identify the exact nature of the surface species, *in situ* diffuse reflectance infrared Fourier transform spectra (DRIFTS) were obtained for 0.6(rGO)@VTiO in methanol-O_2 mixture at 323–473 K (Figure 5E). The bands of physiosorbed methanol (i.e., 2,954 and 2,848 cm^{-1}) and ν(OH) of adsorbed water and/or methanol (3,368 cm^{-1}) were observed at 323 K and then the signal intensity was weakened with temperature. At T > 353 K, the signals of the methoxy species at 2,931 cm^{-1} ($\nu_s(CH_3)$ of the symmetric stretching), 2,825 cm^{-1} ($2\delta_s(CH_3)$ of the Fermi resonance), 1,150 cm^{-1} ($\rho(CH_3)$ of the rocking vibration), 1,441 cm^{-1} ($\delta_{as}(CH_3)$ of the deformation asymmetrical vibrational), and 1,462 cm^{-1} ($\delta_s(CH_3)$ of the deformation symmetrical vibrational) became stronger because the adsorbed methanol dissociated to methoxy groups (Busca et al., 1987). Above 373 K, the bands at 1,584 and 1,562 cm^{-1} (ν_{as}(O–C–O) of formate species), 1,538 and 1,361 cm^{-1} (ν_s(O–C–O) of formate species), 1,482 cm^{-1} ($\delta(CH_2)$ of dimethoxymethane), as well as 1658, 1,633, and 1,205 cm^{-1} (ν(C=O) of adsorbed MF) evinced the formation of CH_2O* and MF (Kaichev et al., 2014) (Whiting et al., 2015). The intensities of MF band at 1,205 cm^{-1} reached the crest at 403 K and then declined at > 423 K probably owing to the formation of CO_2 (2,350 cm^{-1}) (Whiting et al., 2015; Wang et al., 2018b), coinciding with the CO_2 formation in the reaction. No formaldehyde was observed, as the consumption of formaldehyde is a fast step.

Reaction Mechanism over rGO@VTiO Catalysts

To better understand the effects of rGO on the CH_3OH oxidation, the reaction mechanisms with and without rGO were investigated by theoretical calculation. Figure 6A compared the potential energy

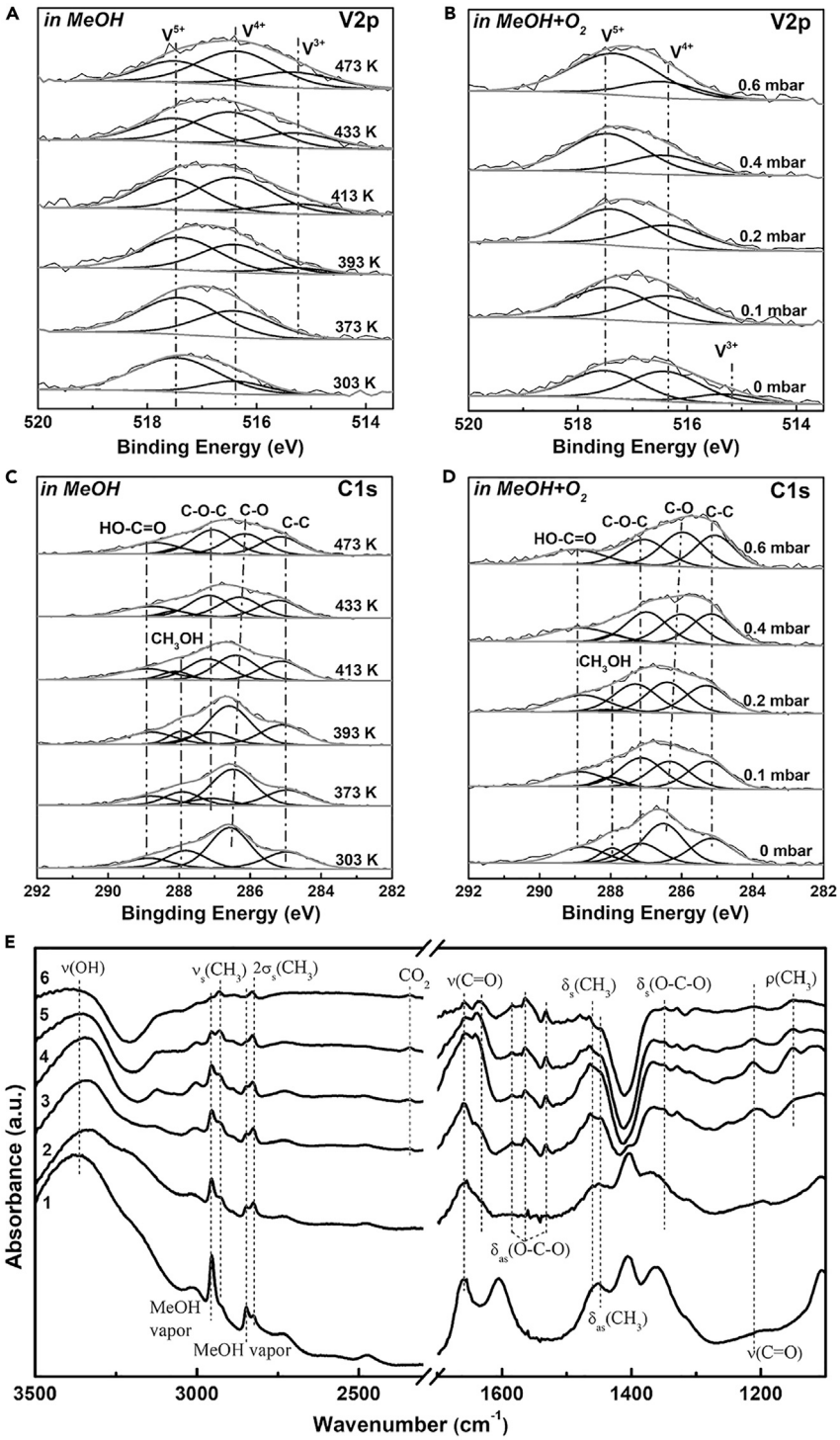

Figure 5. *In Situ* XPS and IR Characterizations of rGO@VTiO Catalysts.

In situ NAP-XPS V2p$_{3/2}$ (A and B) and C1s (C and D) spectra of 0.6(rGO)@VTiO in methanol (A and C) at 323 to 473 K or in CH_3OH (0.4 mbar) -O_2 (0–0.6 mbar) at 403 K (B and D), and (E) *in situ* DRIFTS spectra of the 0.6(rGO)@VTiO in CH_3OH-O_2 mixture at **1**, 323; **2**, 353; **3**, 373; **4**, 403; **5**, 423; and **6**, 473 K.

See also Figures S11–S13 and Tables S7–S13.

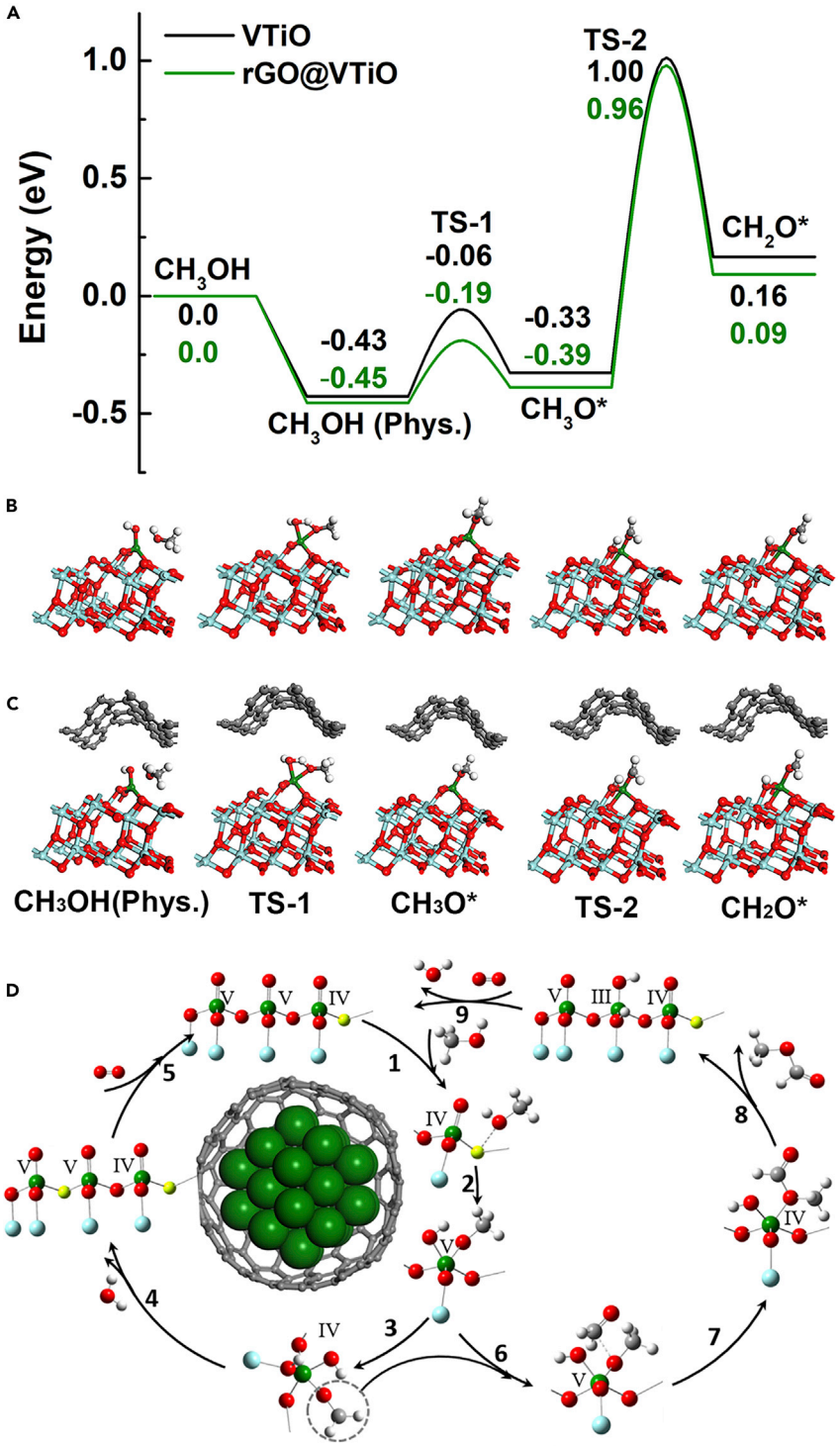

Figure 6. Simulation of Methanol Adsorption on Various Samples

(A–C) (A) Potential energy profiles for CH_3OH to CH_2O^* on the catalyst models; optimized structures of the intermediate states and transition states for VTiO (B) and rGO@VTiO (C).

(D) Possible reaction network for CH_3OH to MF over rGO@VTiO. Color of atoms: C, gray; Ti, blue; V, green; O, red; H, white; OV, yellow.

profiles of CH_3OH oxidation with the intermediate CH_2O*. CH_2O* formation can be divided into three steps (Figures 6B and 6C). CH_3OH is first physiosorbed on the catalyst surface, and the physisorption is slightly stronger on rGO@VTiO than on VTiO (−0.45 eV versus −0.43 eV). The methoxy intermediate (CH_3O*) is then formed by a proton transfer from the OH of the physiosorbed CH_3OH to the terminal OH of the V site, leading to chemisorption and the formation of V-OCH_3 bond. The energy barrier of this step is considerably lower on rGO@VTiO than on VTiO (0.26 versus 0.37 eV), indicating that rGO can promote the chemisorption of CH_3OH. The improved chemisorption of CH_3OH can be attributed to the enhanced acidity and OVs of rGO@VTiO, as indicated by NH_3-TPD and Raman results. Then, further H transfers from the CH_3O* to the bridge -O-V, leading to the formation of CH_2O*. Thus, rGO was predicted to promote chemisorption and activation of CH_3OH.

On combining the experiment and simulation findings, it is justified to explain the methanol oxidation on rGO@VTiO according to the chemical states of V and the roles of rGO. As depicted in Figure 6D, this reaction mainly involves the formation of CH_2O* and MF. For the surface adsorption (step 1), methanol is easily captured by the acidity sites and OVs on rGO@VTiO (Oviedo et al., 2008). Then one proton of the adsorbed methanol transfers to the terminal OH group of V site to form CH_3O*, leading to chemisorption and the formation of $VOCH_3$ bond (step 2), as it has been confirmed by DRIFTS and density functional theory (DFT) methods. In step 3, H of CH_3O* transfers to the O site of V–O–Ti forming Ti–OH along with the reduction of V^{5+} to V^{4+}, as proved by NAP-XPS. Then, CH_3O* transforms into CH_2O* with one H atom recombining with V-OH to form H_2O (step 4). The consumption of CH_2O* and the desorption of H_2O corresponds to the reduction of V^{5+} to V^{4+} and the recovery of OVs. Subsequently, the active sites are re-oxidized from V^{4+} to V^{5+} by O_2 (Step 5), which has been clearly observed from NAP-XPS. This cycle could be expressed as $CH_3OH + 1/2\ O_2 \rightarrow CH_2O^* + H_2O$.

CH_2O* interacts with CH_3O* on the acidic sites of V−OH to form physiosorbed hemiacetal (CH_3OCH_2OH) and V−O bond, and then hemiacetal chemisorbs on the terminal V=O bond to form CH_3OCH_2O−V and HO−V (step 6). The stronger acidity of rGO@VTiO accelerates the formation of hemiacetal. Subsequently, one H of CH_3OCH_2O- transfers to the V–O–Ti site with generating Ti–OH and the adsorbed MF, and concurrently the vanadium cations are reduced from V^{5+} to V^{4+} (step 7). With the desorption of MF, V^{4+} is further reduced to V^{3+} (step 8). These have been proved by *in situ* NAP-XPS and DRIFTS methods. In the end, the V^{3+}/V^{4+} atoms are re-oxidized to V^{5+} by O_2 and the generated H_2O desorbs from the catalyst surface in step 9. The latter cycle is conveyed as $CH_3OH + CH_2O^* + 1/2\ O_2 \rightarrow CH_3OCHO + H_2O$.

DISCUSSION

In summary, the ultrathin rGO layer with well-confined $VTiO_x$ nanoparticles has been realized through a facile co-precipitation and thermal reduction method. The resultant rGO@VTiO demonstrated a superior low-temperature reactivity for the methanol oxidation to high-valued methyl formate in comparison with the rGO-free VTiO catalyst. It exhibited nearly quantitative conversion of methanol to MF with a maximum MF yield of 98.8% at 408 K, even comparable with the noble metal-based catalysts. The reliable stability of rGO@VTiO catalyst was proved by a 500-h testing. Both experimental analyses and computational simulations demonstrate that the presence of a small amount of rGO significantly affects the catalysts in the shell-core interface electronic structure, the surface chemistry of acidity and oxygen vacancies, the methanol adsorption/activation capacity, and the methanol oxidation mechanism. The electron migration between the rGO shell and oxides core significantly reinforced the acidity of rGO@VTiO catalyst in the absence of sulfate groups. This provides a facile method to intensify the highly stable acidity of catalysts not only for VTiO-based catalyst but also for wider solid catalysts, in principle.

Limitations of the Study

The catalyst support is moderately toxic.

Resource Availability

Lead Contact

Further information and requests for resources and reagents should be directed to and will be fulfilled by the Lead Contact, Gaofeng Zeng (zenggf@sari.ac.cn).

Materials Availability

This study did not generate new unique reagents.

Data and Code Availability

The published article includes all datasets/code generated or analyzed during this study.

METHODS

All methods can be found in the accompanying Transparent Methods supplemental file.

SUPPLEMENTAL INFORMATION

Supplemental Information can be found online at https://doi.org/10.1016/j.isci.2020.101157.

ACKNOWLEDGMENTS

We acknowledge the support from the National Natural Science Foundation of China (21506243, 21878322), the Youth Innovation Promotion Association of Chinese Academy of Sciences, the Science and Technology Commission of Shanghai Municipality (19ZR1479200), and the Shanghai Municipal Human Resource and Social Security Bureau.

AUTHOR CONTRIBUTIONS

G.Z. conceived the original idea and drafted the manuscript; the experiments were performed by Y.Z., G.L., and P.W.; L.S. and S.L. performed the computation; all authors have approved to the final version of the manuscript.

DECLARATION OF INTERESTS

The authors declare no competing interests.

Received: February 14, 2020
Revised: April 15, 2020
Accepted: May 7, 2020
Published: June 26, 2020

REFERENCES

Banerjee, A., and Kanan, M.W. (2018). Carbonate-promoted hydrogenation of carbon dioxide to multicarbon carboxylates. Acs Cent. Sci. *4*, 606–613.

Bulushev, D.A., Kiwi-Minsker, L., Rainone, F., and Renken, A. (2002). Characterization of surface vanadia forms on V/Ti-oxide catalyst via temperature-programmed reduction in hydrogen and spectroscopic methods. J. Catal. *205*, 115–122.

Busca, G., Elmi, A.S., and Forzatti, P. (1987). Mechanism of selective methanol oxidation over vanadium oxide-titanium oxide catalysts: a FT-IR and flow reactor study. J. Phys. Chem. *91*, 5263–5269.

Deng, D., Yu, L., Chen, X., Wang, G., Jin, L., Pan, X., Deng, J., Sun, G., and Bao, X. (2013a). Iron encapsulated within pod-like carbon nanotubes for oxygen reduction reaction. Angew. Chem. Int. Ed. *52*, 371–375.

Deng, J., Yu, L., Deng, D.H., Chen, X.Q., Yang, F., and Bao, X.H. (2013b). Highly active reduction of oxygen on a FeCo alloy catalyst encapsulated in pod-like carbon nanotubes with fewer walls. J. Mater. Chem. A *1*, 14868–14873.

Cui, X., Li, H., Wang, Y., Hu, Y., Hua, L., Li, H., Han, X., Liu, Q., Yang, F., He, L., et al. (2018). Room-temperature methane conversion by graphene-confined single iron atoms. Chem *4*, 1902–1910.

Deng, D.H., Chen, X.Q., Yu, L., Wu, X., Liu, Q.F., Liu, Y., Yang, H.X., Tian, H.F., Hu, Y.F., Du, P.P., et al. (2015a). A single iron site confined in a graphene matrix for the catalytic oxidation of benzene at room temperature. Sci. Adv. *1*, e1500462.

Deng, J., Ren, P.J., Deng, D.H., and Bao, X.H. (2015b). Enhanced electron penetration through an ultrathin graphene layer for highly efficient catalysis of the hydrogen evolution reaction. Angew. Chem. Int. Ed. *54*, 2100–2104.

Deng, J., Deng, D., and Bao, X. (2017). Robust catalysis on 2D materials encapsulating metals: concept, application, and perspective. Adv. Mater. *29*, 1606967.

Deng, D.H., Novoselov, K.S., Fu, Q., Zheng, N.F., Tian, Z.Q., and Bao, X.H. (2016). Catalysis with two-dimensional materials and their heterostructures. Nat. Nanotechnol. *11*, 218–230.

Gu, Q.Q., Wen, G.D., Ding, Y.X., Wu, K.H., Chen, C.M., and Su, D.S. (2017). Reduced graphene oxide: a metal-free catalyst for aerobic oxidative desulfurization. Green. Chem. *19*, 1175–1181.

Han, C., Yang, X., Gao, G., Wang, J., Lu, H., Liu, J., Tong, M., and Liang, X. (2014). Selective oxidation of methanol to methyl formate on catalysts of Au–Ag alloy nanoparticles supported on titania under UV irradiation. Green. Chem. *16*, 3603.

Kaichev, V.V., Popova, G.Y., Chesalov, Y.A., Saraev, A.A., Zemlyanov, D.Y., Beloshapkin, S.A., Knop-Gericke, A., Schlögl, R., Andrushkevich, T.V., and Bukhtiyarov, V.I. (2014). Selective oxidation of methanol to form dimethoxymethane and methyl formate over a monolayer V2O5/TiO2 catalyst. J. Catal. *311*, 59–70.

Li, G., Shi, L., Zeng, G., Li, M., Zhang, Y., and Sun, Y. (2015). Sharp molecular-sieving of alcohol-water mixtures over phenyldiboronic acid pillared graphene oxide framework (GOF) hybrid membrane. Chem. Commun. (Camb.) *51*, 7345–7348.

Li, G.H., Zhu, Z.G., Qi, B.Y., Liu, G.J., Wu, P., Zeng, G.F., Zhang, Y.F., Wang, W., and Sun, Y.H. (2016). Rapid capture of Ponceau S via a hierarchical organic-inorganic hybrid nanofibrous membrane. J. Mater. Chem. A *4*, 5423–5427.

Liu, X., Zhou, K., Wang, L., Wang, B., and Li, Y. (2009). Oxygen vacancy clusters promoting reducibility and activity of ceria nanorods. J. Am. Chem. Soc. *131*, 3140–3141.

Liu, Z., Zhang, R., Wang, S., Li, N., Sima, R., Liu, G., Wu, P., Zeng, G., Li, S., and Sun, Y. (2016). Highly efficient and stable vanadia–titania–sulfate catalysts for methanol oxidation to methyl formate: synthesis and mechanistic study. J. Phys. Chem. C *120*, 6591–6600.

Lu, X., Qin, Z., Dong, M., Zhu, H., Wang, G., Zhao, Y., Fan, W., and Wang, J. (2011). Selective oxidation of methanol to dimethoxymethane over acid-modified V2O5/TiO2 catalysts. Fuel *90*, 1335–1339.

Odriozola, J.A., Soria, J., Somorjai, G.A., Heinemann, H., Garcia de La Banda, J.F., lopez Granados, M., and Conesa, J.C. (1991). Adsorption of nitric oxide and ammonia on vanadia-titania catalysts: ESR and XPS studies of adsorption. J. Phys. Chem. *95*, 240–246.

Oviedo, J., Sanchez-De-Armas, R., Miguel, M.A.S., and Sanz, J.F. (2008). Methanol and water dissociation on TiO2 (110): the role of surface oxygen. J. Phys. Chem. C *112*, 17737–17740.

Qi, B., He, X., Zeng, G., Pan, Y., Li, G., Liu, G., Zhang, Y., Chen, W., and Sun, Y. (2017). Strict molecular sieving over electrodeposited 2D-interspacing-narrowed graphene oxide membranes. Nat. Commun. *8*, 825.

Romanyshyn, Y., Guimond, S., Kuhlenbeck, H., Kaya, S., Blum, R.P., Niehus, H., Shaikhutdinov, S., Simic-Milosevic, V., Nilius, N., Freund, H.J., et al. (2008). Selectivity in methanol oxidation as studied on model systems involving vanadium oxides. Top. Catal. *50*, 106–115.

Sima, R., Liu, G., Wang, Q., Wu, P., Qin, T., Zeng, G., Chen, X., Liu, Z., and Sun, Y. (2017). Selective oxidation of methanol to dimethoxymethane at low temperatures through size-controlled VTiOx nanoparticles. ChemCatChem *9*, 1776–1781.

Tang, L., Meng, X., Deng, D., and Bao, X. (2019). Confinement catalysis with 2D materials for energy conversion. Adv. Mater. *31*, e1901996.

Wang, L., Guan, E., Zhang, J., Yang, J., Zhu, Y., Han, Y., Yang, M., Cen, C., Fu, G., Gates, B.C., and Xiao, F.-S. (2018a). Single-site catalyst promoters accelerate metal-catalyzed nitroarene hydrogenation. Nat. Commun. *9*, 1362.

Wang, R., Wu, Z., Chen, C., Qin, Z., Zhu, H., Wang, G., Wang, H., Wu, C., Dong, W., Fan, W., and Wang, J. (2013). Graphene-supported Au-Pd bimetallic nanoparticles with excellent catalytic performance in selective oxidation of methanol to methyl formate. Chem. Commun. (Camb) *49*, 8250–8252.

Wan, J., Chen, W., Jia, C., Zheng, L., Dong, J., Zheng, X., Wang, Y., Yan, W., Chen, C., Peng, Q., et al. (2018). Defect effects on TiO2 nanosheets: stabilizing single atomic site Au and promoting catalytic properties. Adv. Mater. *30*, 1705369.

Wang, Q., Zhang, C., Shi, L., Zeng, G., Zhang, H., Li, S., Wu, P., Zhang, Y., Fan, Y., Liu, G., et al. (2018b). Ultralow Pt catalyst for formaldehyde removal: the determinant role of support. iScience *9*, 487–501.

Wang, Z., Yu, Q., Huang, Y., An, H., Zhao, Y., Feng, Y., Li, X., Shi, X., Liang, J., Pan, F., et al. (2019). PolyCOFs: a new class of freestanding responsive covalent organic framework membranes with high mechanical performance. ACS Cent. Sci. *5*, 1352–1359.

Whiting, G.T., Kondrat, S.A., Hammond, C., Dimitratos, N., He, Q., Morgan, D.J., Dummer, N.F., Bartley, J.K., Kiely, C.J., Taylor, S.H., and Hutchings, G.J. (2015). Methyl formate formation from methanol oxidation using supported gold–palladium nanoparticles. ACS Catal. *5*, 637–644.

Wittstock, A., Zielasek, V., Biener, J., Friend, C.M., and Baumer, M. (2010). Nanoporous gold catalysts for selective gas-phase oxidative coupling of methanol at low temperature. Science *327*, 319–322.

Yang, J., Gong, D., LI, G., Zeng, G., Wang, Q., Zhang, Y., Liu, G., Wu, P., Vovk, E., Peng, Z., et al. (2018). Self-assembly of thiourea-crosslinked graphene oxide framework membranes toward separation of small molecules. Adv. Mater. *30*, e1705775.

Zeng, G., Wang, Y., Gong, D., Zhang, Y., Wu, P., and Sun, Y. (2019). Dual-role membrane as NH3 permselective reactor and azeotrope separator in urea alcoholysis. ACS Cent. Sci. *5*, 1834–1843.

Zhang, C., Wu, P., Liu, G., Zhu, Z., and Zeng, G. (2019). Co-electrospun VTiOx hollow nanofibers for selective oxidation of methanol to high value chemicals. ACS Appl. Nano Mater. *2*, 5224–5232.

Zhang, Q., Li, Y., Zhang, L., Chen, L., Liu, Y., and Lu, Y. (2014a). Structured nanoporous-gold/Al-fiber: galvanic deposition preparation and reactivity for the oxidative coupling of methanol to methyl formate. Green. Chem. *16*, 2992.

Zhang, Q.F., Li, Y.K., Zhang, L., Chen, L., Liu, Y., and Lu, Y. (2014b). Thin-sheet microfibrous-structured nanoporous gold/Al fiber catalysts for oxidative coupling of methanol to methyl formate. J. Catal. *317*, 54–61.

Zhao, H., Bennici, S., Cai, J., Shen, J., and Auroux, A. (2010a). Influence of the metal oxide support on the surface and catalytic properties of sulfated vanadia catalysts for selective oxidation of methanol. J. Catal. *274*, 259–272.

Zhao, H., Bennici, S., Shen, J., and Auroux, A. (2010b). Nature of surface sites of V2O5–TiO2/SO42- catalysts and reactivity in selective oxidation of methanol to dimethoxymethane. J. Catal. *272*, 176–189.

Zhu, Z., Li, G., Zeng, G., Chen, X., Hu, D., Zhang, Y., and Sun, Y. (2015). Fast capture of methyl-dyes over hierarchical amino-Co0.3Ni0.7Fe2O4@SiO2 nanofibrous membranes. J. Mater. Chem. A *3*, 22000–22004.

iScience, Volume *23*

Supplemental Information

Quantitative Conversion of Methanol to Methyl Formate on Graphene-Confined Nano-Oxides

Yelei Zhang, Guojuan Liu, Lei Shi, Ping Wu, Gaofeng Zeng, Chunlei Zhang, Nating Yang, Shenggang Li, and Yuhan Sun

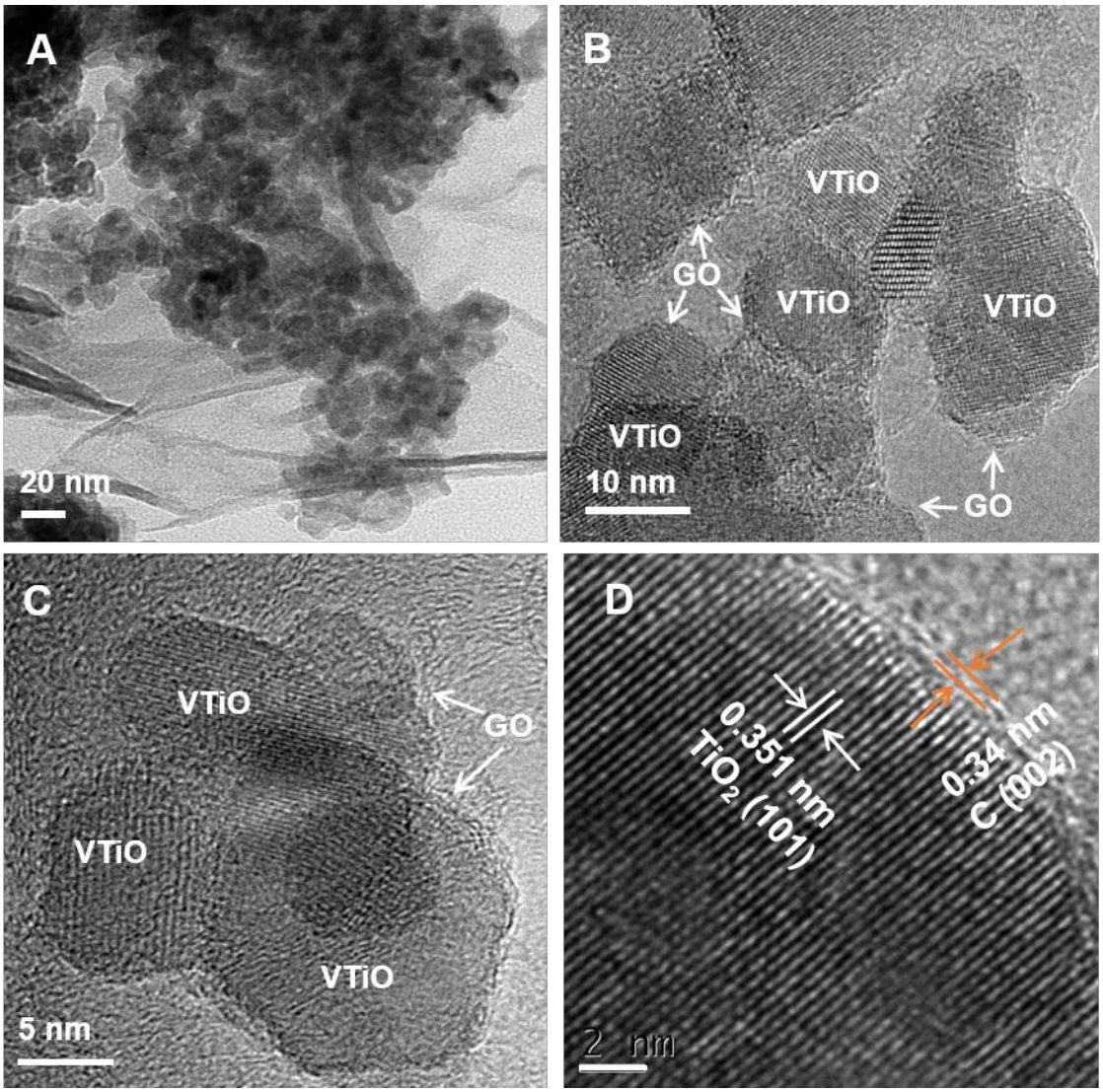

Figure S1. TEM images of 0.6(rGO)@VTiO with different resolutions (related to Figure 1).

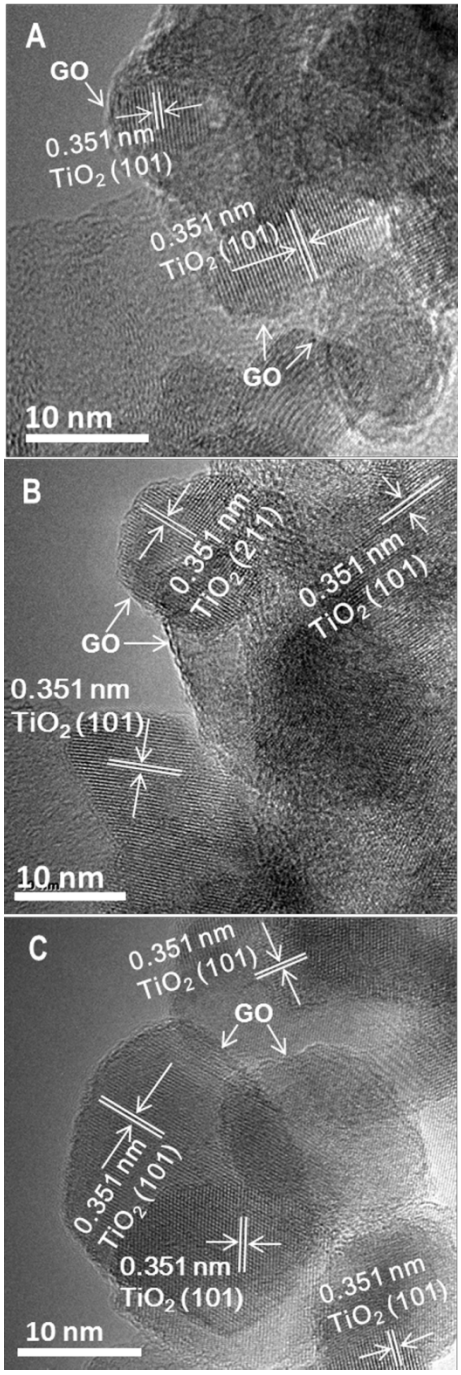

Figure S2. TEM images of 0.3(rGO)@VTiO (A), 1.0(rGO)@VTiO (B) and 2.0(rGO)@VTiO (C) (related to Figure 1).

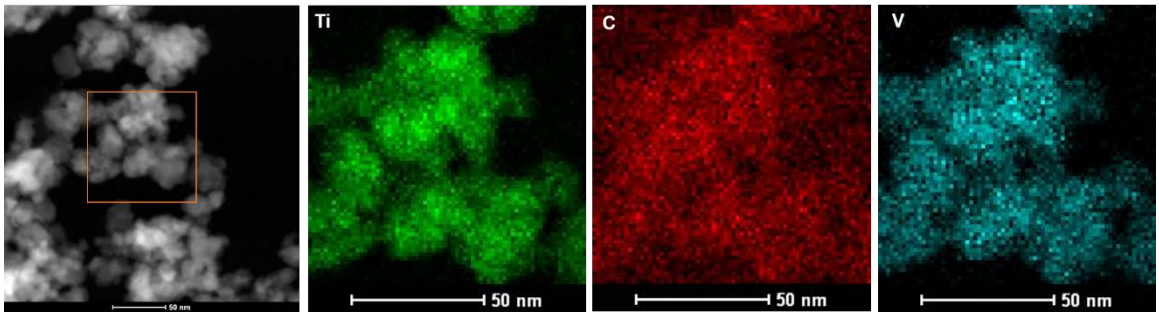

Figure S3. STEM-EDS mapping of Ti, V and C distribution on rGO@VTiO (related to Figure 1).

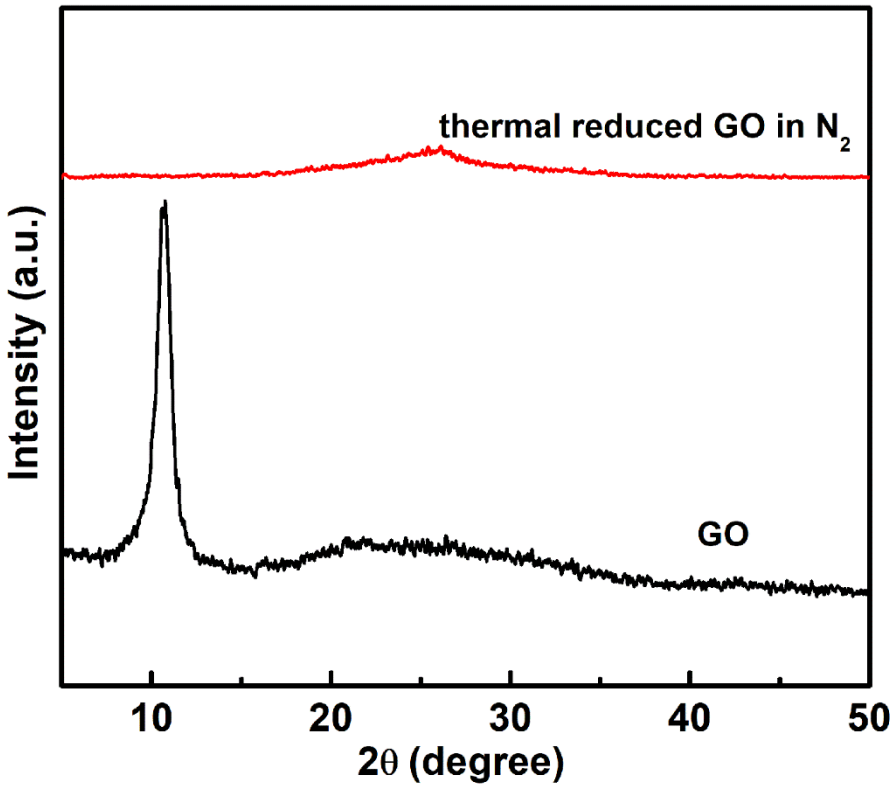

Figure S4. XRD patterns of GO and thermal reduced GO (related to Figure 1).

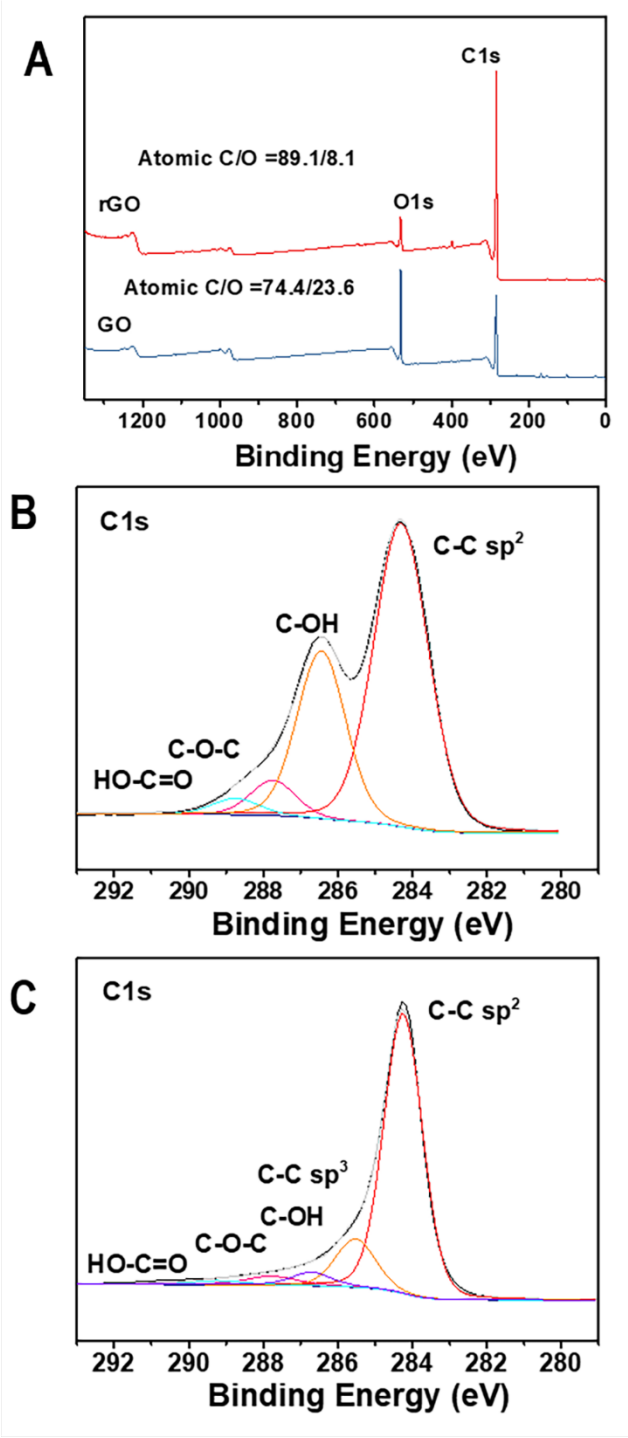

Figure S5. Survey (A) and C1s XPS spectra of GO (B) and reduced GO (C) (related to Figure 1).

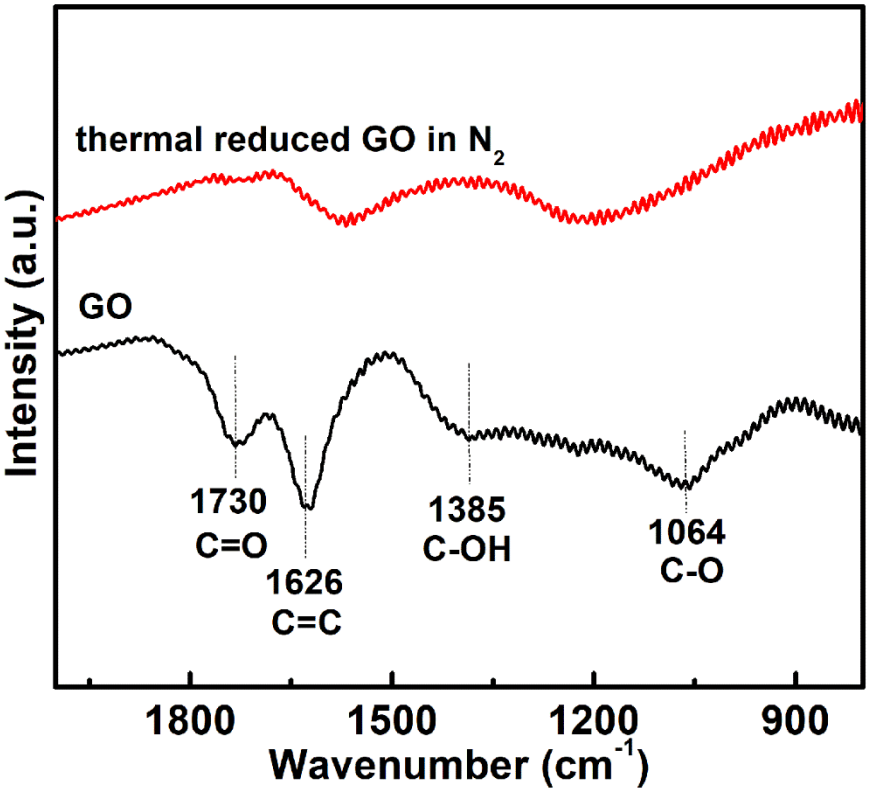

Figure S6. FTIR spectra of GO and reduced GO (related to Figure 1).

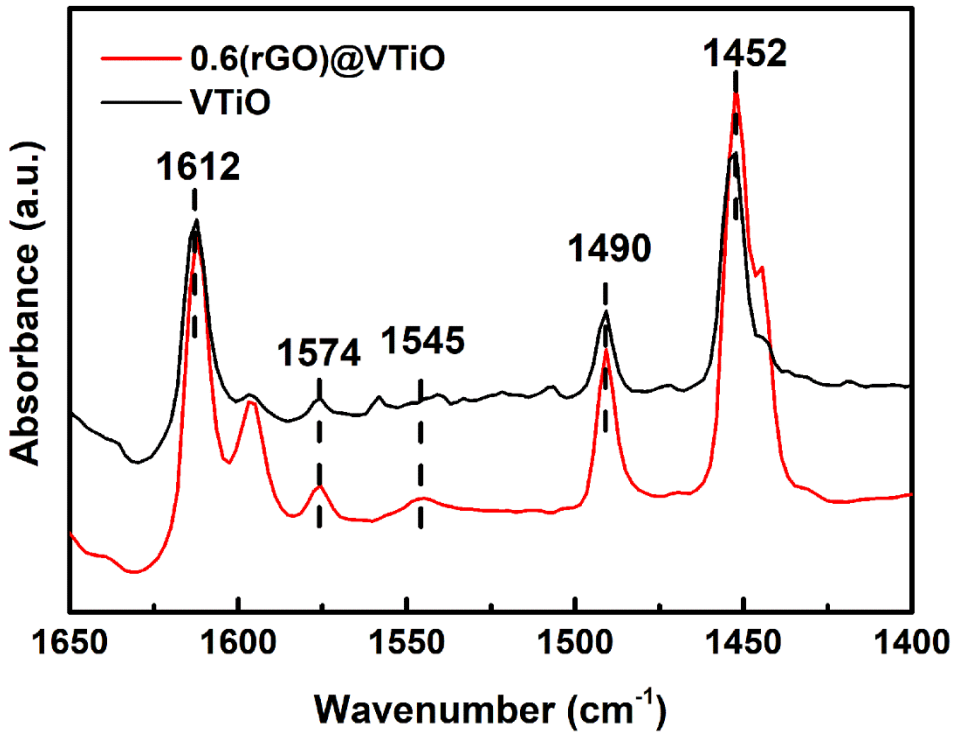

Figure S7. Pyridine adsorption infrared spectra of VTiO and 0.6(rGO)@VTiO (related to Figure 3).

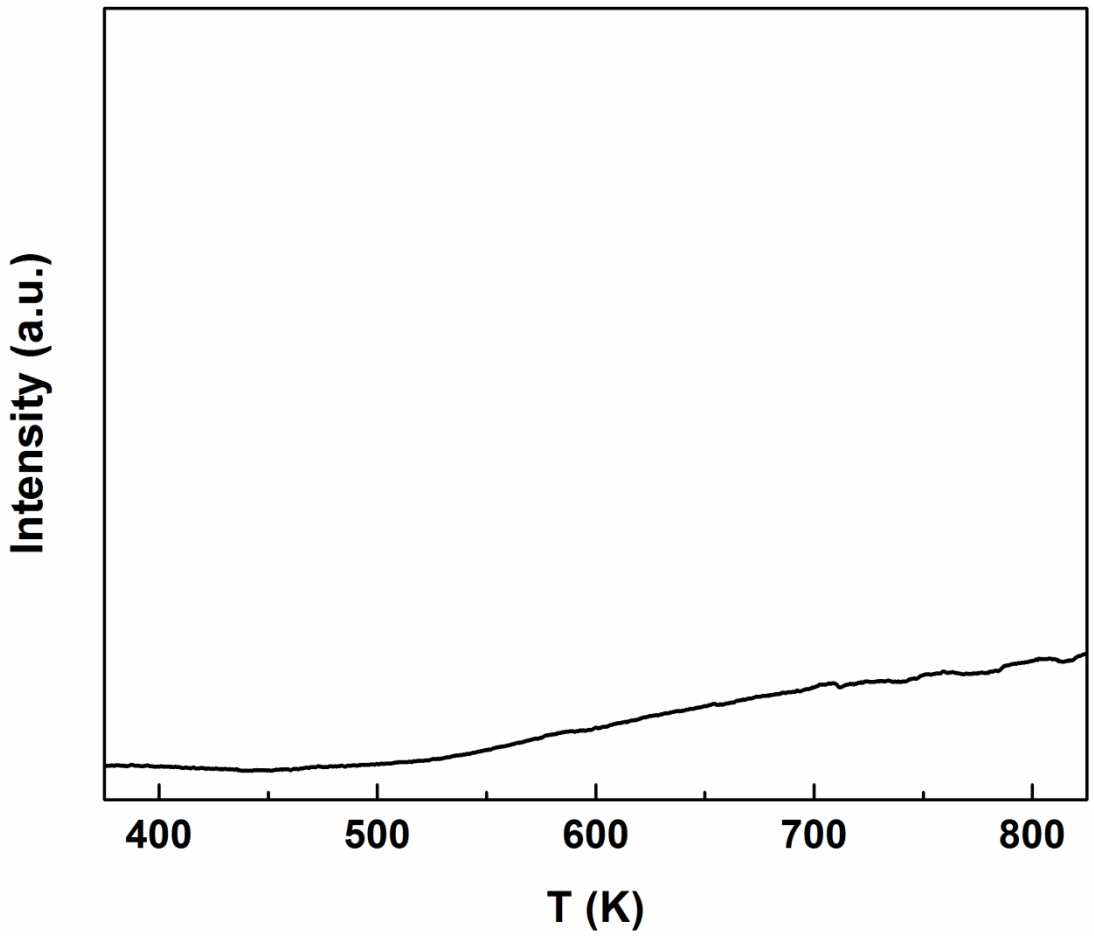

Figure S8 NH_3−TPD profile of rGO sample (related to Figure 3).

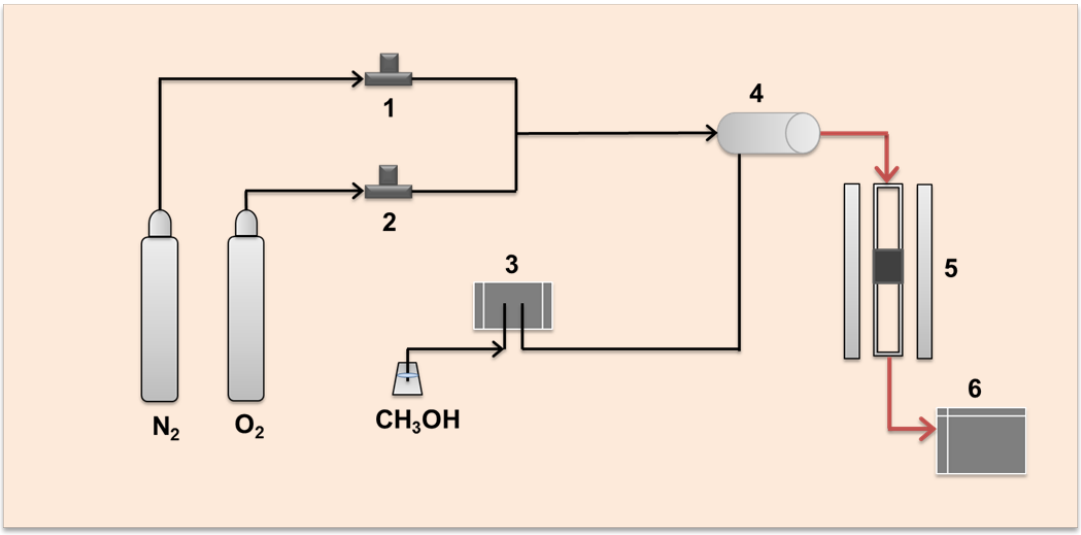

Figure S9. The schematic diagram of online evaluation for methanol oxidation. (1) (1&2) Mass flow controller, (3) P230 Ⅱ high press constant flow pump, (4) Vaporizing chamber, (5) Fixed-bed reactor, and (6) Gas chromatograph. The red line is the gas line kept at 393 K (related to Figure 4).

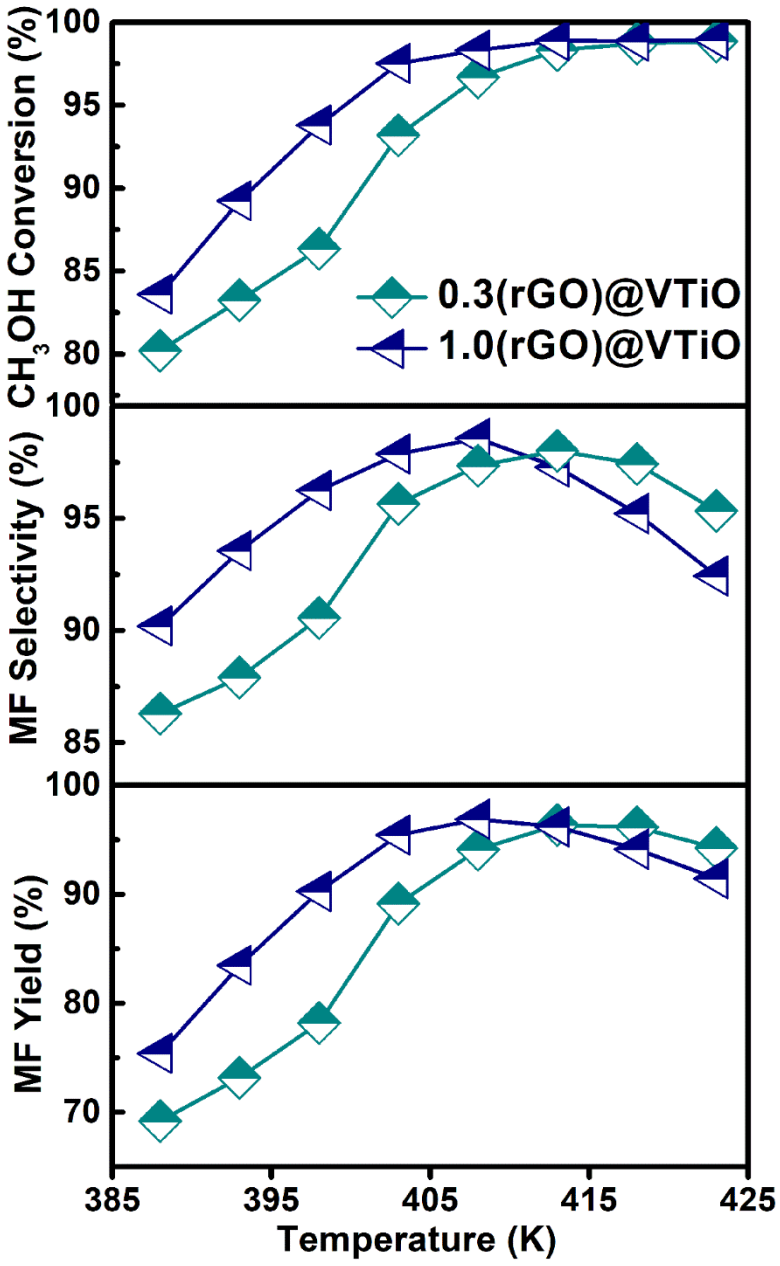

Figure S10. Temperature dependence of methanol to MF on 0.3(rGO)@VTiO and 1.0(rGO)@VTiO catalysts (related to Figure 4).

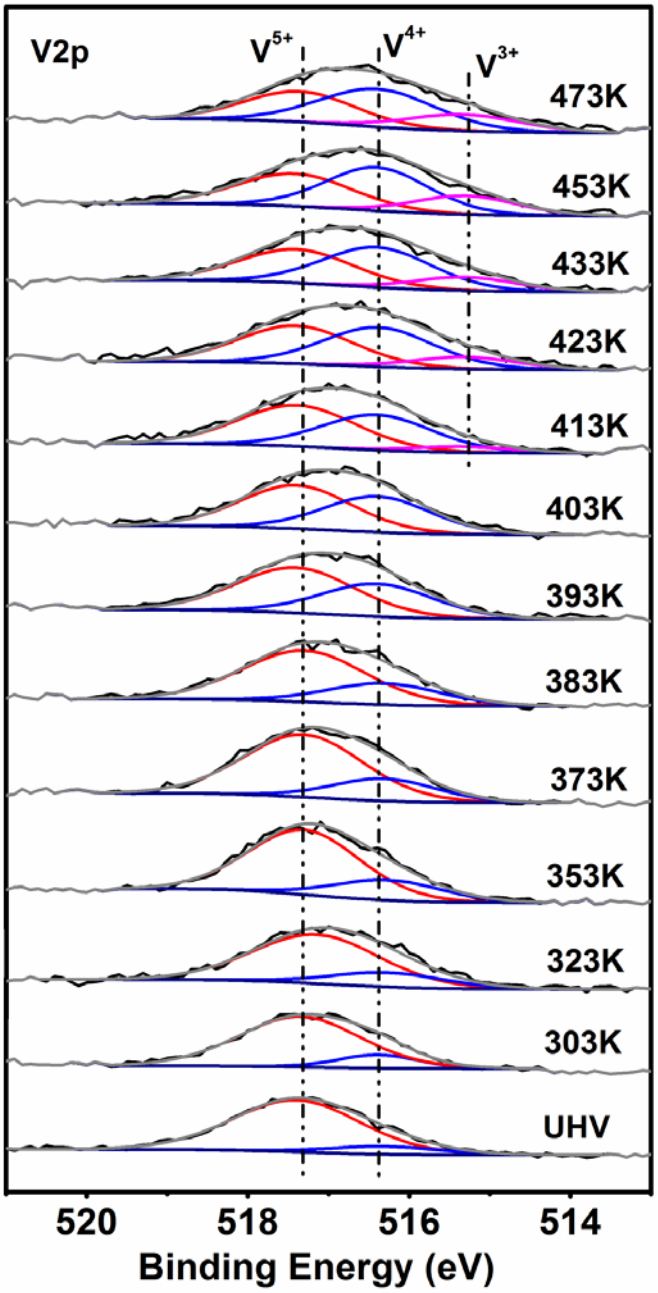

Figure S11. ***In-situ*** **NAP-XPS V2p spectra of VTiO catalyst in ultra-high vacuum (UHV) at room temperature and 0.4 mbar CH_3OH at 303-437 K (related to Figure 5).**

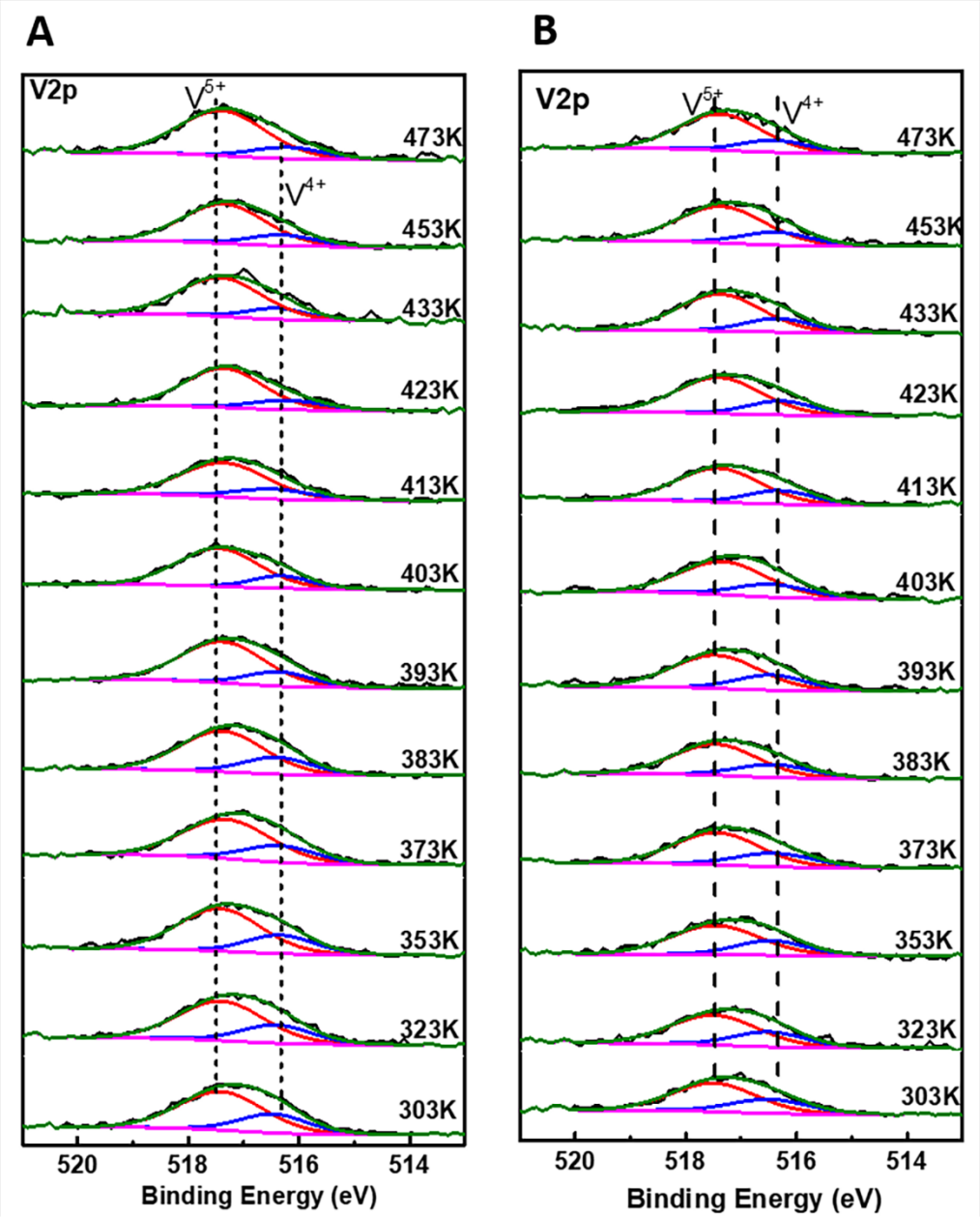

Figure S12. ***In-situ*** **NAP-XPS V2p spectra of VTiO (A) and 0.6(rGO)@VTiO (B) catalyst in 0.4 mbar CH_3OH -0.6 mbar oxygen at 303-437 K (related to Figure 5).**

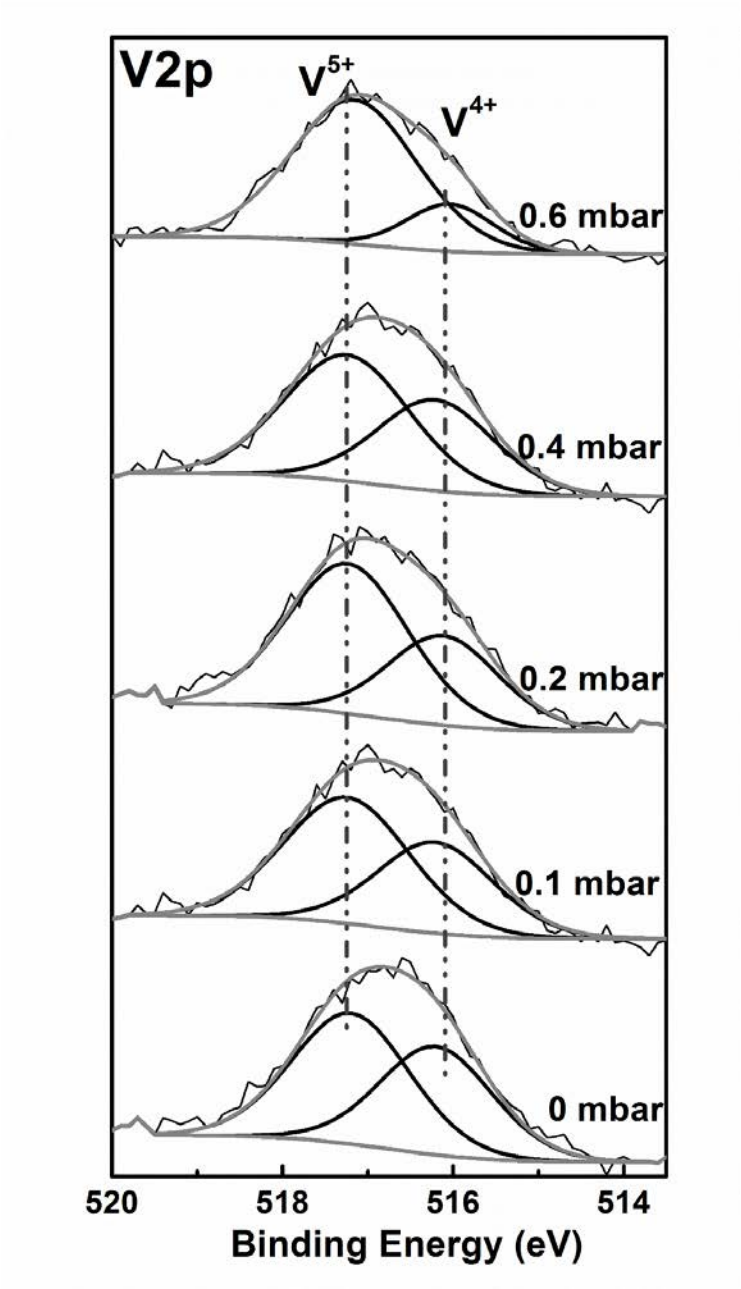

Figure S13. ***In-situ*** **NAP-XPS V2p$_{3/2}$ of VTiO in CH_3OH (0.4 mbar) -O_2 (0-0.6 mbar) at 403 K (related to Figure 5).**

Table S1 The properties of the rGO@VTiO catalysts with different amount of GO (related to Figure 1).

Catalyst	V/Ti (atomic ratio)			S (wt.%)				BET Surface area(m^2/g)
	XPS	EDS	ICP	XPS	EDS	ICP	CHNS elemental analyser	
VTiO	0.41	0.44	0.24	1.45	1.67	1.54	1.78	46
0.3(rGO)@VTiO	0.36	0.40	0.27	0.54	0.62	0.67	0.71	89
0.6(rGO)@VTiO	0.34	0.38	0.28	0	0.04	0.05	0.05	121
1.0(rGO)@VTiO	0.36	0.39	0.29	0	0.02	0.06	0.06	120
2.0(rGO)@VTiO	0.35	0.40	0.31	0	0.03	0.04	0.05	112

Table S2 Binding energies of V2p and the percentages (in atomic%) of vanadia species for VTiO and rGO@VTiO catalysts (related to Figure 2).

Sample	V^{5+} (eV)	V^{4+} (eV)
VTiO	517.4 (78.23%)	516.3 (21.77%)
0.3(rGO)@VTiO	517.4 (69.58%)	516.3 (30.42%)
0.6(rGO)@VTiO	517.4 (66.44%)	516.2 (33.56%)
1.0(rGO)@VTiO	517.5 (71.35%)	516.2 (28.65%)
2.0(rGO)@VTiO	517.5 (73.55%)	516.2 (26.45%)

Table S3 Peak areas of weak acid and medium-strong acid for VTiO and rGO@VTiO catalysts (related to Figure 3).

Catalyst	Weak acid		Medium-strong acid	
	Peak position (K)	Peak Area	Peak position (K)	Peak Area
VTiO	438	808	591	389
0.3(rGO)@VTiO	435	1504	601	946
0.6(rGO)@VTiO	445	1884	606	1324
1.0(rGO)@VTiO	438	1226	636	809
2.0(rGO)@VTiO	432	1206	690	625

Table S4 Peak areas of hydrogen consumption for VTiO and rGO@VTiO catalysts (related to Figure 3).

Catalyst	Weak acid		Medium-strong acid	
	Peak position (K)	Peak Area*100	Peak position (K)	Peak Area*100
VTiO	754	3071	864	50
0.3(rGO)@VTiO	750	2752	868	4
0.6(rGO)@VTiO	720	2634	860	2
1.0(rGO)@VTiO	763	2315	886	3
2.0(rGO)@VTiO	786	2163	896	2

Table S5. Effects of GHSV on the methanol oxidation over 0.6(rGO)@VTiO (P=0.1 MPa，T =408 K， N_2/O_2=9:1，O_2/ CH_3OH =1.5) (related to Figure 4).

GHSV / h^{-1}	Conv.(%)	Selectivity (%)			
	CH_3OH	DMM	FA	DME	MF
1000	99.28	0.00	0.08	0.26	99.66
3000	99.04	0.00	0.16	0.25	99.59
5000	97.94	0.60	1.87	0.35	97.18
8000	80.53	2.08	8.12	0.27	89.53
12000	44.08	12.52	9.60	0.28	77.60

Table S6. Methanol oxidation to MF on various catalysts (related to Figure 4).

Catalyst	T (K)	CH_3OH Conv.(%)	MF Select. (%)	MF Yield (%)	Reference
ReO_x/CeO_2	513	40.0	90.0	36.0	(Liu et al., 2007)
V_2O_5/TiO_2	413	71.0	71.0	49.0	(Liu et al., 2008)
VO_x/TiO_2	433	47.0	57.0	27.0	(Liu et al., 2009)
V_2O_5/TiO_2-SO_4^{2-}	443	95.0	66.0	62.7	(Fan et al., 2015)
V_2O_5/TiO_2-SO_4^{2-}	443	92.0	79.0	73.0	(Zhao et al., 2010)
V_2O_5/TiO_2	393	33.0	14.5	5.0	(Guo et al., 2010b)
VO_x-TiO_2	393	44.0	16.9	7.5	(Guo et al., 2010a)
VO_x/TS-1	423	56.7	16.2	6.2	(Chen et al., 2011)
RuO_x-ZrO_2	373	20.0	96.0	19.2	(Huang et al., 2012)
V_2O_5/TiO_2	413	85.0	82.5	70.1	(Kaichev et al., 2014)
V_2O_5/ZrO_2-Al_2O_3	488	66.0	30.0	20.0	(Zhao et al., 2013)
Pd–Cu/TiO_2	318	50.0	80.0	40.0	(Lisowski et al., 2016)
TiO_2	523	28.0	91.0	26.0	(Kominami et al., 2010)
Au-Ag/TiO_2	293	90.0	85.0	76.5	(Han et al., 2014a, Han et al., 2014b)
Pd-Au/TiO_2 P90	303	83.0	70.0	58.1	(Colmenares et al., 2015)
CuO/CuZnAl	303	98.0	58.0	57.0	(Liu et al., 2016)
Pt/γ-Al_2O_3	295	80.0	40.0	32.0	(Merte et al., 2013)
Au−Pd/TiO_2	303	2.5	100.0	2.5	(Whiting et al., 2015)
Au-Pd/Graphene	343	80.0	100.0	80.0	(Wang et al., 2015)
Au/Al	433	35.0	85.0	30.0	(Zhang et al., 2014b)
Pd/SiO_2	353	88.0	72.0	63.0	(Wojcieszak et al., 2014b)
Pd/Fe_2O_3	353	76.0	81.0	62.0	(Wojcieszak et al., 2014a)
Au-Pd/Graphene	343	90.2	100.0	90.2	(Wang et al., 2013)
Au	353	20.0	97.0	19.4	(Wittstock et al., 2010)
Au/Al-fiber	413	50.0	90.0	45.0	(Zhang et al., 2014a)
rGO@VTiO	403	98.9	99.0	97.9	This Work
	408	99.6	99.2	98.8	This Work

Table S7. V2p XPS of 0.6(rGO)@VTiO in pure methanol atmosphere (related to Figure 5A).

Temp	V^{5+}/eV (content/%)	V^{4+}/eV (content/%)	V^{3+}/eV (content/%)
R.T. UHV	517.4 (75.81)	516.4 (24.19)	–
303K	517.4 (72.99)	516.4 (27.01)	–
323K	517.4 (71.22)	516.3 (28.78)	–
353K	517.4 (70.84)	516.3 (29.16)	–
373K	517.4 (57.40)	516.3 (42.60)	–
383K	517.4 (55.41)	516.3 (44.59)	–
393K	517.4 (51.21)	516.3 (41.10)	515.3 (7.69)
403K	517.4 (41.32)	516.3 (46.08)	515.3 (12.60)
413K	517.4 (38.61)	516.4 (47.39)	515.3 (14.01)
423K	517.5 (32.52)	516.4 (48.45)	515.3 (19.03)
433K	517.4 (31.22)	516.4 (47.63)	515.3 (21.15)
453K	517.4 (28.53)	516.4 (49.52)	515.3 (21.95)
473K	517.4 (26.73)	516.4 (49.95)	515.3 (23.32)

Table S8 V2p XPS of VTiO in pure methanol atmosphere (related to Figure 5).

Temp	V^{5+}/eV (content/%)	V^{4+}/eV (content/%)	V^{3+}/eV (content/%)
UHV	517.3 (88.45)	516.2 (11.55)	
303K	517.2 (85.32)	516.3 (14.68)	
323K	517.2 (79.35)	516.2 (20.65)	–
353K	517.2 (76.79)	516.3 (23.21)	–
373K	517.2 (76.31)	516.1 (23.69)	–
383K	517.2 (72.22)	516.4 (27.78)	–
393K	517.4 (59.28)	516.4 (40.72)	–
403K	517.4 (55.75)	516.4 (44.25)	–
413K	517.4 (51.57)	516.4 (42.18)	515.3 (6.25)
423K	517.4 (43.48)	516.4 (43.86)	515.3 (12.66)
433K	517.4 (40.07)	516.4 (45.57)	515.3 (14.36)
453K	517.4 (37.08)	516.4 (44.07)	515.3 (18.85)
473K	517.4 (34.97)	516.4 (45.76)	515.3 (19.27)

Table S9 Binding energies of V2p and concentration (in atomic%) of vanadia species for 0.6(rGO)@VTiO and VTiO in 0.4 mbar CH_3OH+0.6 mbar O_2 (related to Figure 5).

Condition	rGO@VTiO		VTiO	
	V^{5+}/eV (content/%)	V^{4+}/eV (content/%)	V^{5+}/eV (content/%)	V^{4+}/eV (content/%)
303K	517.4 (69.04)	516.4 (30.96)	517.4 (71.61)	516.4 (28.39)
323K	517.4 (70.68)	516.4 (29.32)	517.4 (72.39)	516.4 (27.61)
353K	517.4 (71.61)	516.4 (28.39)	517.4 (73.66)	516.4 (26.34)
373K	517.4 (72.03)	516.4 (27.97)	517.3 (74.10)	516.3 (25.90)
383K	517.4 (72.89)	516.4 (27.11)	517.4 (74.55)	516.4 (25.45)
393K	517.4 (73.11)	516.4 (26.89)	517.3 (78.78)	516.3 (21.22)
403K	517.4 (75.28)	516.4 (24.72)	517.0 (81.36)	515.9 (18.84)
413K	517.3 (76.11)	516.3 (23.89)	517.0 (81.72)	516.0 (18.28)
423K	517.3 (76.83)	516.3 (23.17)	517.0 (81.98)	515.9 (18.02)
433K	517.4 (77.41)	516.4 (22.59)	517.0 (82.55)	516.0 (17.45)
453K	517.4 (77.78)	516.4 (22.22)	517.4 (82.82)	516.3 (17.18)
473K	517.4 (78.55)	516.4 (21.45)	517.4 (82.84)	516.3 (17.16)

Table S10 XPS fitting results for the 0.6(rGO)@VTiO catalyst in O_2/CH_3OH mixture at 403 K (related to Figure 5).

Conditions	V^{5+}/eV (content/%)	V^{4+}/eV (content/%)	V^{3+}/eV (content/%)
0.4 mbar CH_3OH	517.4 (41.32)	516.3 (46.08)	515.3 (12.60)
0.4 mbar CH_3OH+0.1 mbar O_2	517.4 (55.80)	516.4 (44.20)	–
0.4 mbar CH_3OH+0.2 mbar O_2	517.4 (60.51)	516.4 (39.49)	–
0.4 mbar CH_3OH+0.4 mbar O_2	517.4 (67.69)	516.4 (32.31)	–
0.4 mbar CH_3OH+0.6 mbar O_2	517.3 (75.28)	516.3 (24.72)	–

Table S11 XPS fitting results for the VTiO catalyst in O_2/CH_3OH mixture at 403 K (related to Figure 5).

Conditions	V^{5+}/eV (content/%)	V^{4+}/eV (content/%)	V^{3+}/eV (content/%)
0.4mbar CH_3OH	517.4 (55.75)	516.4 (44.25)	-
0.4mbar CH_3OH+0.1mbar O_2	517.4 (59.91)	516.4 (40.09)	-
0.4mbar CH_3OH+0.2mbar O_2	517.4 (64.63)	516.4 (35.37)	-
0.4mbar CH_3OH+0.4mbar O_2	517.3 (74.10)	516.3 (25.90)	-
0.4mbar CH_3OH+0.6mbar O_2	517.3 (81.36)	516.3 (18.84)	-

Table S12 C1s XPS fitting results for 0.6(rGO)@VTiO in pure methanol (related to Figure 5C).

Condition	C1s, eV （%）				
	MF/Formate	**CH_3OH**	**C-O-C**	**Methoxy**	**C**
303K	288.9 (12.19)	287.8 (19.45)		286.6 (46.08)	285.0 (22.29)
323K	288.9 (11.90)	287.8 (18.68)		286.6 (48.47)	285.0 (20.95)
353K	288.9 (11.84)	287.8 (16.55)	287.1 (3.76)	286.6 (47.61)	285.0 (20.24)
373K	288.9 (11.92)	287.9 (13.88)	287.1 (8.16)	286.5 (45.57)	285.0 (20.47)
383K	288.9 (12.08)	287.9 (12.55)	287.2 (9.95)	286.5 (43.96)	285.0 (21.46)
393K	288.8 (14.61)	287.9 (8.79)	287.1 12.99)	286.6 (41.08)	285.1 (22.52)
403K	288.9 (16.15)	288.0 (8.33)	287.2 (17.24)	286.5 (35.00)	285.1 (23.28)
413K	288.9 (16.97)	288.0 (6.78)	287.2 (24.61)	286.5 (28.96)	285.1 (22.69)
423K	288.9 (17.33)	288.0 (5.49)	287.2 (25.77)	286.4 (27.74)	285.1 (23.68)
453K	288.8 (17.37)	288.1 (5.03)	287.2 (27.97)	286.3 (26.79)	285.2 (22.84)
473K	289.8 (17.49)	288.0 (4.75)	287.7 (29.82)	286.3 (25.53)	285.2 (22.40)

Table S13 C1s XPS fitting results for 0.6(rGO)@VTiO in O_2/CH_3OH mixture at 403 K(related to Figure 5).

Condition	C 1s, eV (%)				
	MF/Formate	**CH_3OH**	**C-O-C**	**Methoxy**	**C**
0.4mbarCH_3OH	288.9 (16.15)	288.0 (8.33)	287.2 (17.24)	286.5 (35.00)	285.1 (23.28)
0.4mbarCH_3OH+0.1mbarO_2	288.9 (16.31)	288.0 (5.81)	287.1 (28.47)	286.3 (24.46)	285.2 (24.95)
0.4mbarCH_3OH+0.2mbarO_2	288.9 (17.43)	288.0 (5.15)	287.1 (28.26)	286.2 (24.01)	285.2 (25.15)
0.4mbarCH_3OH+0.4mbarO_2	290.0 (18.03)	288.0 (3.96)	287.1 (26.45)	286.2 (25.34)	285.3 (26.22)
0.4mbarCH_3OH+0.6mbarO_2	290.0 (18.40)		287.2 (23.90)	286.1 (30.72)	285.2 (26.98)

Transparent Methods

Catalyst synthesis

The catalysts were prepared by a co-precipitation method. Typically, 3.4 g $VOSO_4$, 15.0 g $TiSO_4$ and 7.4 g H_2SO_4 (>98 wt.%) were dissolved in sequence in deionized water and then mixed with 0 -100 mL GO suspension (1mg GO mL^{-1}, LEVSON Shanghai) to obtain a 580 mL solution. Then the pH value was adjusted to 9.3 by dropping a diluted ammonia solution (3.7 wt.% $NH_3 \cdot H_2O$) into the solution in an ice-water bath. The precipitate was then filtered and washed after 2 h aging. The solid was dried at 393 K overnight and calcined in N_2 for 6 h at 673 K. As a reference, rGO was prepared by heating GO precursor in N_2 for 6 h at 673 K.

Catalytic oxidation of methanol

Methanol oxidation was carried out in a tubular fixed-bed reactor (I.D. 8 mm) under atmospheric pressure (Figure S13). 1.0 g catalyst (20-40 mesh) mixed with quartz sand was packed in the center of the reactor. The catalysts were firstly treated in 10 v.% O_2 / 90v.%N_2 at 388 K for 0.5 h. Then methanol was fed into the reactor through a vaporizer at 388 K by a constant flow pump. The reaction products were analyzed by two series-connected on-line gas chromatography (Shimazu GC−2014) with TCD detectors. Methanol, dimethoxymethane, MF, formaldehyde, dimethyl ether and water were analyzed with a Porapak T column, while O_2, N_2, CO_2 and CO were analyzed with Porapak N and MS-13X columns. The gas lines between reactor and GCs were kept at 393 K.

Computational Methods

All optimization calculations were carried out with the Vienna ab initio simulation program (VASP) using the Perdew-Burke-Ernzerhof (PBE) exchange-correlation functional. The projector-augmented wave (PAW) method was used to describe electron-ion interactions. Spin polarization were

applied, and the plane wave energy cut-off was set to 400 eV with a force convergence of 0.05 eV $Å^{-1}$. The VTiO catalysts were modelled by a supercell of the anatase TiO_2 (101) surface slab model with the lateral dimension of 10.38 Å × 7.68 Å with a vacuum layer of 20 Å, and with the addition of a $VO_2(OH)$ cluster the composition of the supercell is $VTi_{16}O_{35}$.(Shapovalov et al., 2012) The rGO@VTiO catalyst were modeled by adding a graphene layer consisting of 36 C atoms on top of the VTiO catalyst model, and relaxation of the structure yields a distance of 7.6 Å between the TiO_2 surface and the graphene layer, although the space between the $VO_2(OH)$ cluster and the graphene layer is less. The bottom half of the TiO_2 slab were fixed at their bulk positions. The Brillouin zone was sampled with a k-point grid of (4 × 3 × 1). We applied the Hubbard U correction with the method of Dudarev and the U_{eff} values of 2.3 eV for Ti and 2.0 eV for V.(Lutfalla et al., 2011) The Grimme's D3 empirical dispersion correction with the Becke-Johnson damping method (D3-BJ) was applied improve the description of the van der Waals interaction between the graphene layer and the slab surface.(Grimme et al., 2011) The climbing image-nudged elastic band method and the force-reversed method were used to locate the transition states.(Henkelman et al., 2000)

Characterizations

The crystal structure of catalysts was determined by XRD (Rigaku Ultima IV) using Cu Kα radiation (λ= 0.15406 nm, 40 kV, 40 mA). The morphology of the catalysts was characterized by transmission electron microscopy (TEM, JEM-2100, 200 kV) and scanning electron microscopy (SEM, Zeiss SUPRA 55 SAPPHIRE, 2-20 kV). The surface areas of the samples were derived from N_2 sorption carried out on an automatic micropore physisorption analyser (TriStar II 3020). The subsurface elemental distribution of catalysts was measured by energy dispersive spectrometers (EDS, Oxford Instrument) attached to SEM and TEM. The elemental composition of catalysts

was measured with inductively coupled plasma atomic emission spectrometry (ICP-AES, PerkinElmer Optima 8000). The near-surface chemistry of the catalysts was analysed by X-ray photoelectron spectroscopy (XPS, K-Alpha, Al Kα radiation, 1486.6 eV, 12 kV, 3mA). *In situ* DRIFTS were recorded by Thermo Fisher 6700. Raman spectroscopy measurements were performed using a Renishaw Raman spectrometer using a 12.5 mW laser source at an excitation wavelength of 532 nm. A Micromeritics AutoChem II 2920 apparatus, equipped with a thermal conductivity detector (TCD), was used for H_2-TPR analysis. NH_3-TPD was performed in a fix-bed reactor. Pyridine adsorption infrared spectra (Py-FTIR) were recorded on a Nicolet-6700 FT-IR spectrophotometer with a DTGS detector. The spectra were obtained in the 4000–400 cm^{-1} range with a resolution of 2 cm^{-1} and 128 scans. Self-supporting wafer (10–30 mg, 13 mm diameter) was first evacuated at 623 K for 30 min and then exposed to pyridine at 333 K for 5 min. Desorption of pyridine was carried out by evacuation for 30 min at 423 K. The *in-situ* NAP-XPS was carried out on the spectrometer equipped with PHOIBOS semi spherical electron energy analysis, focusing (spot size ~300 μm) monochromatized (Al Kα) X-ray light source and IQE-11A ion gun and infrared laser heater (SPECS Co.).

Supplemental Reference

CHEN, S., WANG, S., MA, X. & GONG, J. 2011. Selective oxidation of methanol to dimethoxymethane over bifunctional VO(x)/TS-1 catalysts. *Chem Commun (Camb)*, 47**,** 9345-7.

COLMENARES, J. C., LISOWSKI, P., LOMOT, D., CHERNYAYEVA, O. & LISOVYTSKIY, D. 2015. Sonophotodeposition of Bimetallic Photocatalysts Pd-Au/TiO2: Application to Selective Oxidation of Methanol to Methyl Formate. *Chemsuschem*, 8**,** 1676-1685.

FAN, Z., GUO, H., FANG, K. & SUN, Y. 2015. Efficient V2O5/TiO2composite catalysts for dimethoxymethane synthesis from methanol selective oxidation. *RSC Adv.*, 5**,** 24795-24802.

GRIMME, S., EHRLICH, S. & GOERIGK, L. 2011. Effect of the Damping Function in Dispersion Corrected Density Functional Theory. *Journal of Computational Chemistry*, 32**,** 1456-1465.

GUO, H., LI, D., JIANG, D., LI, W. & SUN, Y. 2010a. Characterization and performance of sulfated VOx–TiO2 catalysts in the one-step oxidation of methanol to dimethoxymethane. *Catalysis Communications*, 11**,** 396-400.

GUO, H., LI, D., JIANG, D., XIAO, H., LI, W. & SUN, Y. 2010b. Characterization and performance of

V2O5–TiO2 catalysts prepared by rapid combustion method. *Catalysis Today,* 158**,** 439-445.

HAN, C., YANG, X., GAO, G., WANG, J., LU, H., LIU, J., TONG, M. & LIANG, X. 2014a. Selective oxidation of methanol to methyl formate on catalysts of Au–Ag alloy nanoparticles supported on titania under UV irradiation. *Green Chemistry,* 16**,** 3603.

HAN, C. H., YANG, X. Z., GAO, G. J., WANG, J., LU, H. L., LIU, J., TONG, M. & LIANG, X. Y. 2014b. Selective oxidation of methanol to methyl formate on catalysts of Au-Ag alloy nanoparticles supported on titania under UV irradiation. *Green Chemistry,* 16**,** 3603-3615.

HENKELMAN, G., UBERUAGA, B. P. & JONSSON, H. 2000. A climbing image nudged elastic band method for finding saddle points and minimum energy paths. *Journal of Chemical Physics,* 113**,** 9901-9904.

HUANG, H., LI, W. Z. & LIU, H. C. 2012. Effect of treatment temperature on structures and properties of zirconia-supported ruthenium oxide catalysts for selective oxidation of methanol to methyl formate. *Catalysis Today,* 183**,** 58-64.

KAICHEV, V. V., POPOVA, G. Y., CHESALOV, Y. A., SARAEV, A. A., ZEMLYANOV, D. Y., BELOSHAPKIN, S. A., KNOP-GERICKE, A., SCHLöGL, R., ANDRUSHKEVICH, T. V. & BUKHTIYAROV, V. I. 2014. Selective oxidation of methanol to form dimethoxymethane and methyl formate over a monolayer V2O5/TiO2 catalyst. *Journal of Catalysis,* 311**,** 59-70.

KOMINAMI, H., SUGAHARA, H. & HASHIMOTO, K. 2010. Photocatalytic selective oxidation of methanol to methyl formate in gas phase over titanium(IV) oxide in a flow-type reactor. *Catalysis Communications,* 11**,** 426-429.

LISOWSKI, P., COLMENARES, J. C., LOMOT, D., CHERNYAYEVA, O. & LISOVYTSKIY, D. 2016. Preparation by sonophotodeposition method of bimetallic photocatalysts Pd-Cu/TiO2 for sustainable gaseous selective oxidation of methanol to methyl formate. *Journal of Molecular Catalysis a-Chemical,* 411**,** 247-256.

LIU, J., HAN, C. H., YANG, X. Z., GAO, G. J., SHI, Q. Q., TONG, M., LIANG, X. Y. & LI, C. F. 2016. Methyl formate synthesis from methanol on titania supported copper catalyst under UV irradiation at ambient condition: Performance and mechanism. *Journal of Catalysis,* 333**,** 162-170.

LIU, J., ZHAN, E., CAI, W., LI, J. & SHEN, W. 2007. Methanol Selective Oxidation to Methyl Formate over ReOx/CeO2 Catalysts. *Catalysis Letters,* 120**,** 274-280.

LIU, J. L., ZHAN, E. S., CAI, W. J., LI, J. & SHEN, W. J. 2008. Methanol selective oxidation to methyl formate over ReOx/CeO2 catalysts. *Catalysis Letters,* 120**,** 274-280.

LIU, J. W., SUN, Q., FU, Y. C. & SHEN, J. Y. 2009. Preparation and characterization of mesoporous VOx-TiO2 complex oxides for the selective oxidation of methanol to dimethoxymethane. *Journal of Colloid and Interface Science,* 335**,** 216-221.

LUTFALLA, S., SHAPOVALOV, V. & BELL, A. T. 2011. Calibration of the DFT/GGA plus U Method for Determination of Reduction Energies for Transition and Rare Earth Metal Oxides of Ti, V, Mo, and Ce. *Journal of Chemical Theory and Computation,* 7**,** 2218-2223.

MERTE, L. R., AHMADI, M., BEHAFARID, F., ONO, L. K., LIRA, E., MATOS, J., LI, L., YANG, J. C. & ROLDAN CUENYA, B. 2013. Correlating Catalytic Methanol Oxidation with the Structure and Oxidation State of Size-Selected Pt Nanoparticles. *Acs Catalysis,* 3**,** 1460-1468.

SHAPOVALOV, V., FIEVEZ, T. & BELL, A. T. 2012. A Theoretical Study of Methanol Oxidation Catalyzed

by Isolated Vanadia Clusters Supported on the (101) Surface of Anatase. *Journal of Physical Chemistry C,* 116**,** 18728-18735.

WANG, R., WU, Z., CHEN, C., QIN, Z., ZHU, H., WANG, G., WANG, H., WU, C., DONG, W., FAN, W. & WANG, J. 2013. Graphene-supported Au-Pd bimetallic nanoparticles with excellent catalytic performance in selective oxidation of methanol to methyl formate. *Chem Commun (Camb),* 49**,** 8250-2.

WANG, R. Y., WU, Z. W., WANG, G. F., QIN, Z. F., CHEN, C. M., DONG, M., ZHU, H. Q., FAN, W. B. & WANG, J. G. 2015. Highly active Au-Pd nanoparticles supported on three-dimensional graphene-carbon nanotube hybrid for selective oxidation of methanol to methyl formate. *Rsc Advances,* 5**,** 44835-44839.

WHITING, G. T., KONDRAT, S. A., HAMMOND, C., DIMITRATOS, N., HE, Q., MORGAN, D. J., DUMMER, N. F., BARTLEY, J. K., KIELY, C. J., TAYLOR, S. H. & HUTCHINGS, G. J. 2015. Methyl Formate Formation from Methanol Oxidation Using Supported Gold-Palladium Nanoparticles. *Acs Catalysis,* 5**,** 637-644.

WITTSTOCK, A., ZIELASEK, V., BIENER, J., FRIEND, C. M. & BAUMER, M. 2010. Nanoporous Gold Catalysts for Selective Gas-Phase Oxidative Coupling of Methanol at Low Temperature. *Science,* 327**,** 319-322.

WOJCIESZAK, R., GHAZZAL, M. N., GAIGNEAUX, E. M. & RUIZ, P. 2014a. Low temperature oxidation of methanol to methyl formate over Pd nanoparticles supported on gamma-Fe2O3. *Catalysis Science & Technology,* 4**,** 738-745.

WOJCIESZAK, R., KARELOVIC, A., GAIGNEAUX, E. M. & RUIZ, P. 2014b. Oxidation of methanol to methyl formate over supported Pd nanoparticles: insights into the reaction mechanism at low temperature. *Catalysis Science & Technology,* 4**,** 3298-3305.

ZHANG, Q., LI, Y., ZHANG, L., CHEN, L., LIU, Y. & LU, Y. 2014a. Structured nanoporous-gold/Al-fiber: galvanic deposition preparation and reactivity for the oxidative coupling of methanol to methyl formate. *Green Chemistry,* 16**,** 2992.

ZHANG, Q. F., LI, Y. K., ZHANG, L., CHEN, L., LIU, Y. & LU, Y. 2014b. Thin-sheet microfibrous-structured nanoporous gold/Al fiber catalysts for oxidative coupling of methanol to methyl formate. *Journal of Catalysis,* 317**,** 54-61.

ZHAO, H., BENNICI, S., SHEN, J. & AUROUX, A. 2010. Nature of surface sites of V2O5–TiO2/SO42- catalysts and reactivity in selective oxidation of methanol to dimethoxymethane. *Journal of Catalysis,* 272**,** 176-189.

ZHAO, Y., QIN, Z., WANG, G., DONG, M., HUANG, L., WU, Z., FAN, W. & WANG, J. 2013. Catalytic performance of V2O5/ZrO2–Al2O3 for methanol oxidation. *Fuel,* 104**,** 22-27.